CMS Physics Analysis Summary

Contact: cms-pag-conveners-susy@cern.ch 2013/05/31

Phenomenological MSSM interpretation of the CMS 2011 5fb^{-1} results

The CMS Collaboration

Abstract

We interpret within the phenomenological MSSM (pMSSM) results obtained by CMS using a pp data set collected in 2011 at 7 TeV, corresponding to an integrated luminosity of 5 fb^{-1}. The pMSSM is a 19-parameter realization of the MSSM defined at the SUSY scale, that captures most of the features of the general R-parity conserving weak-scale MSSM. A global Bayesian analysis is performed that yields posterior probability densities of model parameters, masses and observables. We provide conclusions that are more generic, and therefore more robust, than those derived in more constrained setups, including simplified models and models that impose particular SUSY breaking schemes, such as the CMSSM. We also study implications for the MSSM Higgs sector, as well as for dark matter searches. Furthermore, we discuss which scenarios currently escape detection despite a high production cross section. Our study thus gives a coherent global picture of how the current CMS searches constrain supersymmetry in general.

Contents

1 Introduction

The recent discovery [1, 2] of a new particle with properties consistent with a Standard Model (SM) Higgs boson is clearly the most significant news from the Large Hadron Collider (LHC). The other significant news from the LHC is, unfortunately, the absence of any compelling sign of new physics. In particular, there is no hint of supersymmetry (SUSY), one of the most thoroughly studied ideas for physics beyond the Standard Model (BSM) (see, for example, Refs. [3, 4] for recent reviews).

The absence of evidence, however, may not be evidence of absence. Searches for SUSY have typically been interpreted within constrained models with just a few parameters. A commonly used model is the Constrained Minimal Supersymmetric Standard Model (CMSSM), which is characterized by four parameters and a sign [5, 6]: a universal scalar mass m_0, a gaugino mass $m_{1/2}$ and a trilinear coupling A_0 defined at the GUT scale, $M_{\text{GUT}} \sim 10^{16}$ GeV, together with $\tan\beta$ and sign($^-$). The simplifying assumption of universality at the GUT scale has served a useful purpose: for many years it has provided a framework for gauging progress in SUSY searches. However, many mass patterns and signatures that are *a priori* possible in the MSSM cannot be realized in the CMSSM. Neither are they accounted for in Simplified Model Spectra (SMS) [7]. The drawback of interpreting the experimental results in the $(m_0, m_{1/2})$ plane or within SMS topologies is the risk of imposing overly strong constraints on SUSY that are not warranted by observations.

In order to be more general, *i.e.* to account fully for the plethora of mass patterns and decay

modes that can occur in the MSSM, it is necessary to pursue a less model-dependent approach. In this paper we therefore use a 19-dimensional realization of the MSSM called the *phenomenological MSSM* (pMSSM) [8], which captures most of the phenomenological features of the R-parity conserving MSSM. In the pMSSM, all MSSM parameters are specified at the electroweak scale and allowed to vary freely subject to the requirement that the model be consistent with electroweak symmetry breaking and other such basic constraints. Since the pMSSM includes neither relations between SUSY breaking terms at a high scale, nor large correlations between sparticle masses from renormalization group evolution, the scenarios not currently explored using LHC data are different from those in, *e.g.*, the CMSSM and related GUT-scale models.

To explore the pMSSM, we use a representative subset of the results obtained by CMS based on the 7 TeV data set collected in 2011, corresponding to an integrated luminosity of 5 fb^{-1}, to assess what the data tell us, and do not tell us, about SUSY.[1] Our study is an extension of the pioneering work of Ref. [9], which interpreted three independent CMS analyses based on 1 fb^{-1} of data—the α_T hadronic [10], the same-sign dilepton [11] and the opposite-sign dilepton [12] analyses—in terms of the pMSSM, confirming that this approach is both feasible and better at obtaining general conclusions about supersymmetry. Note that the diversity of phenomena covered by the pMSSM is also helpful in suggesting new approaches to searching for SUSY at the LHC.

The present study follows closely the Bayesian approach (see for example [13, 14]) of Ref. [9]. Prior to this work, the parameter space of the pMSSM was studied in detail in Refs. [15–17]. A Bayesian study of the pMSSM was conducted in Ref. [18] before LHC data were available. A somewhat different study, in which the CMSSM gluino–squark mass limits based on 1 fb^{-1} of LHC data were used in a dark matter global fit of a 9-parameter version of the MSSM, was performed in Ref. [19]. Another analysis using the 1 fb^{-1} CMS results [10–12], but based on flat random scans of the pMSSM parameter space, was presented in Ref. [20]. Our study thus represents the first global analysis of how the 7 TeV CMS results constrain the MSSM in general, while aiming to make as few assumptions as possible.

The paper is organized as follows. The definition of the pMSSM is given in Section 2. It is followed by the description of our analysis in Section 3, which includes the construction of the model prior in Section 3.1, and the calculation of the CMS likelihoods in Section 3.2. Our results are presented in Section 4, including discussions of the impact of the 5 fb^{-1} CMS searches and their current sensitivity to the pMSSM. Section 5 contains our conclusions.

More details on the analysis and its results, consequences for the Higgs sector and for dark matter observables, as well as a discussion of the scenarios that are missed by the current searches are given in a series of appendices.

2 Definition of the Phenomenological MSSM (pMSSM)

A priori, the weak-scale MSSM has 120 free parameters, assuming that R-parity is conserved (to avoid proton decay and to ensure that the lightest SUSY particle, the LSP, is stable) and assuming that the gravitino is heavy. This is clearly too much for any phenomenological study. However, most of these parameters are associated with CP-violating phases and, or, flavor changing neutral currents (FCNC), which are severely constrained by experiment. A few reasonable assumptions about the flavor and CP structure therefore allow us to reduce the number of free parameters by a factor 6, without imposing any SUSY breaking scheme. Working with parameters defined at the weak scale is indeed of great advantage for our purpose because

[1] The analysis of the full 8 TeV data set is underway.

models of SUSY breaking always introduce relations between the soft terms that need not to hold in general.

Concretely, the only generic way to satisfy very strong constraints on CP violation is to take all parameters to be real. FCNC constraints are satisfied in a generic way by taking all sfermion mass matrices and trilinear couplings to be flavor-diagonal. Moreover, the first two generations of sfermions are taken to be degenerate. Regarding the trilinear A-terms of the first two generations, these only enter phenomenology multiplied by the associated very small Yukawa couplings and are thus not experimentally relevant. Only the 3rd generation parameters A_t, A_b and A_τ have consequences that are potentially observable.

This leaves us with 19 real, weak-scale SUSY Lagrangian parameters — the so-called phenomenological MSSM, or pMSSM for short [8]. As mentioned, the pMSSM captures most of the phenomenological features of the R-parity conserving MSSM and, most importantly, encompasses and goes beyond a broad range of more constrained SUSY models. The free parameters of the pMSSM are the following:

- the gaugino mass parameters M_1, M_2, and M_3;
- the ratio of the Higgs vacuum expectation values (VEV) $\tan\beta = v_2/v_1$;
- the higgsino mass parameter μ and the pseudo-scalar Higgs mass m_A;
- 10 sfermion mass parameters $m_{\tilde{F}}$, where $\tilde{F} = \tilde{Q}_1, \tilde{U}_1, \tilde{D}_1, \tilde{L}_1, \tilde{E}_1, \tilde{Q}_3, \tilde{U}_3, \tilde{D}_3, \tilde{L}_3, \tilde{E}_3$ (imposing degeneracy of the first two generations $m_{\tilde{Q}_1} \equiv m_{\tilde{Q}_2}$, $m_{\tilde{L}_1} \equiv m_{\tilde{L}_2}$, etc.), and
- the trilinear couplings A_t, A_b and A_τ ,

in addition to the SM parameters. To minimize theoretical uncertainties in the Higgs sector, these parameters are conveniently defined at the scale, $M_{\rm SUSY} \equiv \sqrt{m_{\tilde{t}_1} m_{\tilde{t}_2}}$, often also referred to as the electroweak symmetry breaking (EWSB) scale.

The pMSSM parameter space is constrained by a number of theoretical requirements. First, the sparticle spectrum must be free of tachyons and cannot lead to color or charge breaking minima in the scalar potential. We also require that EWSB be consistent and that the Higgs potential be bounded from below. Finally, in this study, we also require that the LSP be the lightest neutralino, $\tilde{\chi}_1^0$.

This leaves us with a model that is an excellent proxy for the full MSSM with a sufficiently small number of parameters such that a complete exploration of it is possible given existing computer resources. For computing the physical masses and interactions to state-of-the-art accuracy, we use `SoftSUSY_3.3.1` [21] as the spectrum generator, with the input parameters defined at $M_{\rm SUSY}$. Thus the spectrum calculation includes 1-loop corrections for sparticle masses and mixings, as well as 2-loop corrections for the light Higgs boson mass.

3 Analysis

3.1 Construction of the pMSSM prior

The purpose of this study is to assess what current data tell us, and do not tell us, about the MSSM using the more tractable pMSSM as a proxy. Using these data we perform a global Bayesian analysis that yields posterior probability densities of model parameters, masses and

observables. We work within the pMSSM sub-space,

$$\begin{gathered}
-3\,\text{TeV} \leq M_1, M_2 \leq 3\,\text{TeV} \\
0 \leq M_3 \leq 3\,\text{TeV} \\
-3\,\text{TeV} \leq \mu \leq 3\,\text{TeV} \\
0 \leq m_A \leq 3\,\text{TeV} \\
2 \leq \tan\beta \leq 60 \\
0 \leq \tilde{Q}_{1,2}, \tilde{U}_{1,2}, \tilde{D}_{1,2}, \tilde{L}_{1,2}, \tilde{E}_{1,2}, \tilde{Q}_3, \tilde{U}_3, \tilde{D}_3, \tilde{L}_3, \tilde{E}_3 \leq 3\,\text{TeV} \\
-7\,\text{TeV} \leq A_t, A_b, A_\tau \leq 7\,\text{TeV},
\end{gathered} \tag{1}$$

of the model (i.e., input) parameter set described in Section 2. A point in this space will be denoted by θ. In addition, we work in the unbounded SM parameter space defined by m_t, $m_b(m_b)$ and $\alpha_s(M_Z)$ in which the SM parameters are constrained with a likelihood. For each pMSSM point, we use `SoftSUSY_3.3.1` [21] to compute the SUSY spectrum, `SuperIso_v3.3` [22] to compute the low-energy constraints, and `micrOMEGAs_2.4.5` [23–25] to compute the dark matter relic density $\Omega_{\tilde{\chi}_1^0}h^2$, direct detection cross sections and to check compatibility with various pre-LHC sparticle mass limits. Moreover, we use `SUSYHIT (SDECAY1.3b, HDECAY3.4)` [26] to produce SUSY and Higgs decay tables. The various codes are interfaced using the SUSY Les Houches Accord [27].

The sub-space defined in Eq. (1) was chosen to be as large as is needed to cover the range of sparticle masses to which the LHC might conceivably be ultimately sensitive. The lower bound of 2 for $\tan\beta$ was chosen so as to avoid any issues of non-perturbativity for the top-quark Yukawa coupling after evolution up to the GUT scale. Typically, perturbativity becomes a very serious issue for $\tan\beta \lesssim 1.7$.

The posterior density of θ given data D is given by

$$p(\theta|D) \sim L(D|\theta)\, p(\theta), \tag{2}$$

where $L(D|\theta)$ is the likelihood and $p(\theta)$ is the prior probability density, or prior for short. Since we consider multiple independent measurements D_i, the combined likelihood is given by $L(D|\theta) = \prod_i L(D_i|\theta)$. The prior encodes any knowledge we have about θ independent of the measurements D_i. It may for example encode information from measurements other than D_i or theoretical assumptions.

We partition the data into two parts: *i*) the preCMS-measurements (preCMS) listed in Table 1 and *ii*) the CMS SUSY and Exotica search results (CMS) listed in Table 2. With this partitioning, the posterior density becomes

$$p(\theta|D) \sim L(D^{\text{CMS}}|\theta)\, L(D^{\text{preCMS}}|\theta)\, p_0(\theta) = L(D^{\text{CMS}}|\theta)\, p^{\text{preCMS}}(\theta), \tag{3}$$

where $p_0(\theta)$ is the prior at the start of the inference chain[2] and $p^{\text{preCMS}}(\theta) \sim L(D^{\text{preCMS}}|\theta)\, p_0(\theta)$ can be viewed as a prior that encodes the information from the preCMS-measurements. This partitioning allows us to assess the impact of the CMS results on the pMSSM parameter space while being consistent with constraints from the previous measurements.

In addition to the experimental results included in our calculation of the prior $p^{\text{preCMS}}(\theta)$, Table 1 lists the corresponding likelihood $L(D_j^{\text{preCMS}}|\mu_j(\theta))$ for each observable j, where $\mu_j(\theta)$

[2] Recently, this prior has been referred to as the *ur-prior* from the German prefix *ur* meaning original or primitive (Glen Cowan).

Table 1: The measurements that are the basis of our pMSSM prior $p^{\text{preCMS}}(\theta)$. All measurements except the measurement of m_h at the LHC were used to sample points from the pMSSM parameter space via Markov Chain Monte Carlo (MCMC). The m_h likelihood was imposed as a weight on the sampled points.

i	Observable $\mu_j(\theta)$	Constraint D_j^{preCMS}	Likelihood function $L(D_j^{\text{preCMS}}\|\mu_j(\theta))$	MCMC / post-MCMC
1	$BR(b \to s\gamma)$ [28, 29]	$(3.55 \pm 0.23^{\text{stat}} \pm 0.24^{\text{th}} \pm 0.09^{\text{sys}}) \times 10^{-4}$	Gaussian	MCMC
2a	$BR(B_s \to \mu\mu)$ [30]	observed CLs curve from [30]	$d(1-CLs)/d(BR(B_s \to \mu\mu))$	MCMC
2b	$BR(B_s \to \mu\mu)$ [31]	$3.2^{+1.5}_{-1.2} \times 10^{-9}$	2-sided Gaussian	post-MCMC
3	$R(B_u \to \tau\nu)$[32]	1.63 ± 0.54	Gaussian	MCMC
4	Δa_μ [33]	$(26.1 \pm 8.0^{\text{exp}} \pm 10.0^{\text{th}}) \times 10^{-10}$	Gaussian	MCMC
5	m_t [34]	$173.3 \pm 0.5^{\text{stat}} \pm 1.3^{\text{sys}}$ GeV	Gaussian	MCMC
6	$m_b(m_b)$ [32]	$4.19^{+0.18}_{-0.06}$ GeV	Two-sided Gaussian	MCMC
7	$\alpha_s(M_Z)$ [32]	0.1184 ± 0.0007	Gaussian	MCMC
8a	m_h	pre-LHC: $m_h^{low} = 112$	1 if $m_h \geq m_h^{low}$ 0 if $m_h < m_h^{low}$	MCMC
8b	m_h	LHC: $m_h^{low} = 120$, $m_h^{up} = 130$	1 if $m_h^{low} \leq m_h \leq m_h^{up}$ 0 if $m_h < m_h^{low}$ or $m_h > m_h^{up}$	post-MCMC
9	sparticle masses	LEP [35] (via micrOMEGAs [23–25])	1 if allowed 0 if excluded	MCMC
10	prompt $\tilde{\chi}_1^\pm$	$c\tau(\tilde{\chi}_1^\pm) < 10$ mm	1 if allowed 0 if excluded	post-MCMC

denotes the model prediction for the observable j, such as $BR(b \to s\gamma)$ or m_h, for a given θ. We obtained a discrete representation of the prior $p^{\text{preCMS}}(\theta)$ within the sub-space defined in Eq. (1) by sampling points from $p^{\text{preCMS}}(\theta)$ using a Markov Chain Monte Carlo (MCMC) method [36]. We take the prior $p_0(\theta)$ at the start of the inference chain to be flat, i.e. $p(\theta) = \text{constant}$[3]. By construction, this method produces a sample of points whose density in the neighborhood of θ is $\propto p^{\text{preCMS}}(\theta)$. Since we have chosen the prior $p_0(\theta) = \text{constant}$, the sampled points also constitute a discrete representation of the preCMS likelihood as a function of the pMSSM parameters θ. The experimental results and bounds 1, 2a, 3 – 8a and 9 in Table 1 were included in the preCMS likelihood used in the MCMC scan. Condition 8b was imposed post-MCMC to take into account, approximately, the measured mass of the new particle [1, 2] identified as the low-mass Higgs boson, h. During the course of this study, a first measurement of $BR(B_s \to \mu\mu)$ was presented by the LHCb Collaboration [37]. We have taken this measurement into account by reweighting each sampled point by the ratio of the new $BR(B_s \to \mu\mu)$ likelihood, 2b, to the the old likelihood, 2a, in Table 1.

Approximately 20 million points were sampled from the pMSSM sub-space, using multiple MCMC chains, from which a random sub-sample of 7205 points were selected subject to the flat prior $120 \leq m_h \leq 130$ GeV. This prior, which brackets the measured mass of the new particle, is wide enough to permit a study of the influence of the constraints on the mass of the neutral Higgs boson, h, on the posterior densities. It also allows for the still significant uncertainty in the theoretical prediction for the Higgs boson mass.

For each point in the sub-sample of 7205 points, we calculated the predictions $\mu_l(\theta)$ for the observables measured in the CMS analyses listed in Section 3.2 and the associated likelihoods $L(D_l^{\text{CMS}}|\mu_l(\theta))$, where D_l^{CMS} denotes the CMS data associated with the prediction $\mu_l(\theta)$.

One feature of the pMSSM that requires attention is the following. Letting M_1, M_2 and μ, vary freely over the same range implies that about 2/3 of the time M_2 or μ will be the smallest mass parameter in the neutralino mass matrix. This implies that in a considerable portion of the pMSSM parameter space the $\tilde{\chi}_1^\pm$ and $\tilde{\chi}_2^0$ are close in mass or almost degenerate with the $\tilde{\chi}_1^0$ [38]. When the $\tilde{\chi}_1^\pm$–$\tilde{\chi}_1^0$ mass difference becomes very small, the charginos are long-lived and can traverse the detector before they decay. Investigating such scenarios thoroughly requires dedicated searches involving lost tracks, dE/dx or time of flight measurements, which is outside the scope of this study. We therefore impose a model prior that restricts our study to scenarios with prompt charginos, where by prompt we mean a particle with an average proper lifetime of $c\tau < 10$ mm. Appendix A explains how the $\tilde{\chi}_1^\pm$-$\tilde{\chi}_1^0$ degeneracy arises. The probability distributions of selected pMSSM parameters and sparticle masses after imposing various preCMS requirements are presented in Appendix B.

3.2 Construction of CMS likelihoods

The experimental results of all CMS analyses considered in this study are event counts in a variety of signal regions. In the following, we describe how the predictions $\mu_l(\theta)$ and the CMS likelihoods $L(D_l^{\text{CMS}}|\mu_l(\theta))$ are computed. The expected signal counts, $s_l(\theta)$, for each pMSSM point is calculated as follows. For a given pMSSM parameter point θ, we

- generate 10000 events using `PYTHIA6` [39],

[3] An alternative approach would be to start with an adequate approximation to a 19-dimensional reference prior, which would minimize the effect of the arbitrariness of the prior choice by maximizing, on average, the influence of the data. But, the development of a computationally practical algorithm is a work in progress. We have repeated our analysis by sampling from a class of power-law priors and we find that the conclusions given in Section 5 are robust with respect to this class of priors.

- simulate the response of the CMS detector to these events, using a fast simulation of the CMS detector, and
- analyze these events in order to arrive at the expected signal counts $s_l(\theta)$.

Since the experimental results are event counts, we assume the likelihood to be a Poisson distribution,

$$L(D_l^{CMS}|\mu_l(\theta)) = \text{Poisson}(N_l|s_l(\theta) + b_l), \tag{4}$$

with observed count N_l and expected count $s_l(\theta) + b_l$ ($\equiv \mu_l(\theta)$), where b_l is the expected background count [4] for the l^{th} experimental result [5]. In the current study, we neglect the uncertainty in these predictions. In effect, we assume δ-function priors for the expected signals. However, we repeat the calculations with the signal predictions varied by $\pm 50\%$.

The information about each background parameter b_l is given by the background estimate B_l and its associated uncertainty δB_l. This information can be encoded in an evidence-based prior [40], $p(b_l|B_l, \delta B_l)$, modeled with a gamma density obtained as follows. Suppose that by construction the ratio of the expected count in a control region, for example a side-band, to the expected background count, b_l, in the signal region is K_l. From the count Q_l in the control region, the background in the signal region can be estimated using $B_l = Q_l/K_l$, with an associated uncertainty $\delta B_l = \sqrt{Q_l}/K_l$. Then the likelihood of the count Q_l is just $\text{Poisson}(Q_l|K_l b_l)$. Given a flat prior for $K_l b_l$, we obtain a posterior density for $K_l b_l$ whose form will be a gamma density in b_l [6].

$$p(b_l|B_l, \delta B_l) = \text{Gamma}(b_l; Q_l + 1, K_l), \tag{5}$$

where $\text{Gamma}(x; \alpha, \beta) = \beta \exp(-\beta x)(\beta x)^{\alpha-1}/\Gamma(\alpha)$, $Q_l \equiv (B_l/\delta B_l)^2$, and $K_l \equiv B_l/\delta B_l^2$. For each pMSSM point, and for each CMS experimental result, we compute the marginal likelihood

$$p(N_l|s_l(\theta)) = \int \text{Poisson}(N_l|s_l(\theta) + b_l)\, p(b_l|B_l, \delta B_l) db_l, \tag{6}$$

by an exact integration [41] over the expected background b_l. For disjoint experimental results, the overall CMS likelihood $L(D^{\text{CMS}}|\theta)$ is simply the product

$$L(D^{\text{CMS}}|\theta) = \prod_l p(N_l|s_l(\theta)). \tag{7}$$

The posterior density $p(\theta|D^{\text{CMS}}) \propto L(D^{\text{CMS}}|\theta)\, p(\theta)$ is approximated by weighting each sampled pMSSM point by $L(D^{\text{CMS}}|\theta)$. The posterior density is normalized to unity over the pMSSM sub-space given in Eq. (1).

3.3 Implementation of CMS analyses

We list in Table 2 the CMS analyses we have implemented in this study. These analyses, which are a subset of the 7 TeV CMS SUSY analyses, cover a variety of final states.

The goal is to test different regions of the pMSSM parameter space, characterized by different admixtures of final state topologies. The hadronic $H_T + H_T^{miss}$ search is expected to have the greatest sensitivity over the pMSSM space. It is an inclusive analysis based on ≥ 3 jets and missing transverse energy that targets gluino and squark production with long hadronic

[4] In fact, the expected background count also depends on the SM parameters, but for simplicity we neglect this dependence.

[5] We use lower-case letters for parameters and upper-case letters for measured or known quantities.

[6] Note that Q_l is not necessarily an integer. Moreover, had we used the reference prior for a Poisson distribution rather than a flat prior, the argument of the gamma density would be $Q + 1/2$ rather than $Q + 1$.

Table 2: List of implemented CMS analyses, which are used for building the CMS likelihood $L(D^{\text{CMS}}|\theta)$.

Analysis	CERN doc. no & reference
Hadronic $H_T + H_T^{miss}$ search	CMS-SUS-12-011 [42]
Hadronic $H_T + E_T^{miss} + b$-jets search	CMS-SUS-12-003 [43]
Hadronic $H_T + E_T^{miss} + \tau$s search	CMS-SUS-12-004 [44]
Hadronic monojet $+E_T^{miss}$ search	CMS-EXO-11-059 [45]
Leptonic same sign (SS) 2ℓ search	CMS-SUS-11-010 [46]
Leptonic opposite sign (OS) 2ℓ search	CMS-SUS-11-011 [47]
Leptonic electroweakino (EWKino) search	CMS-SUS-12-006 [48]

cascades. The hadronic $H_T + E_T^{miss} + b$-jets search that involves $\geq$ 3 jets and $\geq$ 1 b-jet primarily focuses on gluinos decaying to hadronic 3rd generation particles, while the hadronic $H_T + E_T^{miss} + \tau$s search looks for τs that are produced in $\tilde{\chi}^0$ decays in gluino cascades. The hadronic monojet $+E_T^{miss}$ search, which features a single high-p_T jet and missing transverse energy, probes final states in which the visible contribution comes not from sparticle decays directly, but from the associated jet production via initial state radiation. Example cases include compressed spectra and dark matter pair production. The leptonic searches involving SS 2ℓ and OS 2ℓ look for leptonic decays of charginos, neutralinos and sleptons in gluino cascades. Such final states with energetic leptons and jets occur in only a few percent of the pMSSM parameter space. Finally, the leptonic electroweakino search targets neutralino-chargino pair production with leptonic decays by probing final states with multiple leptons and missing energy.

Each of the analyses of Table 2 provides results for a number of search regions. When these search regions are disjoint, we combine the results by taking the product of the likelihoods calculated for each search region. We do not take into account the correlation in systematic uncertainties across multiple search regions. In the end we provide the posterior distributions for each analysis separately, presenting the combined result for the analysis when the search regions are disjoint, or presenting the results for individual search regions when the search regions overlap.

The observed event counts N_l and SM background estimates $B_l \pm \delta B_l$, which are taken from the official results of these analyses, are listed in Tables 3 to 11 in Appendix C.

4 Results

4.1 Impact of the CMS searches

In this section, we present the posterior densities for various MSSM masses and the total SUSY production cross section before and after inclusion of the results of the CMS analyses described in Section 3. Figures 1–3 show the 1D posterior densities for the $\tilde{g}$, $\tilde{u}_R$, $\tilde{t}_1$, $\tilde{b}_1$, $\tilde{\chi}_1^0$, $\tilde{\chi}_2^0$, $\tilde{\chi}_1^\pm$ masses, comparing the preCMS distributions (shown as filled blue histograms) to the distributions after incorporating the results of various CMS analyses (shown as line histograms). For each analysis, different signal (that is, search) regions are combined if they are exclusive, or shown separately otherwise. Solid curves represent the posterior densities obtained from likelihoods calculated using the central values of predicted signal counts $s(\theta)$, whereas dashed and dotted lines represent the posterior densities obtained from likelihoods calculated using $s - 0.5s$ and $s + 0.5s$, respectively. A 50% uncertainty in s is a conservative estimate of the overall statistical, systematic and theoretical uncertainties.

Our results show that the analyses with the greatest effect on the distributions are the hadronic search $H_T + H_T^{miss}$ followed by the hadronic searches $H_T + E_T^{miss} + b$-jets and monojet $+E_T^{miss}$. The hadronic search $H_T + E_T^{miss} + \tau$s and leptonic searches SS 2ℓ, OS 2ℓ and electroweakino (EWKino) 3ℓ have no visible impact, with the EWKino being the most sensitive among the leptonic analyses. This pattern of impact is generally valid for all masses and variables, with the greatest impact being on the gluino and squark mass distributions, since gluino and squark production is dominant at the LHC for the pMSSM.

Figure 1 shows the effect of three representative analyses, namely the hadronic $H_T + H_T^{miss}$, the hadronic $H_T + E_T^{miss} + b$-jets and the leptonic EWKino on the gluino mass. The hadronic searches favor higher $\tilde{g}$ masses, except for the 2BT ($2b$-jets + tight H_T) search region defined by $H_T > 600$ GeV, $E_T^{miss} > 300$ GeV and $N_{b\text{-jets}} \geq 2$ of the $H_T + E_T^{miss} + b$-jets search, which prefers lower gluino masses. The latter is due to a 2.2σ excess observed in that channel [43] with which the predictions of models with light gluinos decaying to b-jets are consistent[7]. For the $\tilde{u}_R$ squark, shown in Fig. 2 (and likewise for the $\tilde{u}_L$ and $\tilde{d}_{R,L}$ squarks, though not shown here) higher mass values are favored except for the 2BT search region of the $H_T + E_T^{miss} + b$-jets analysis.

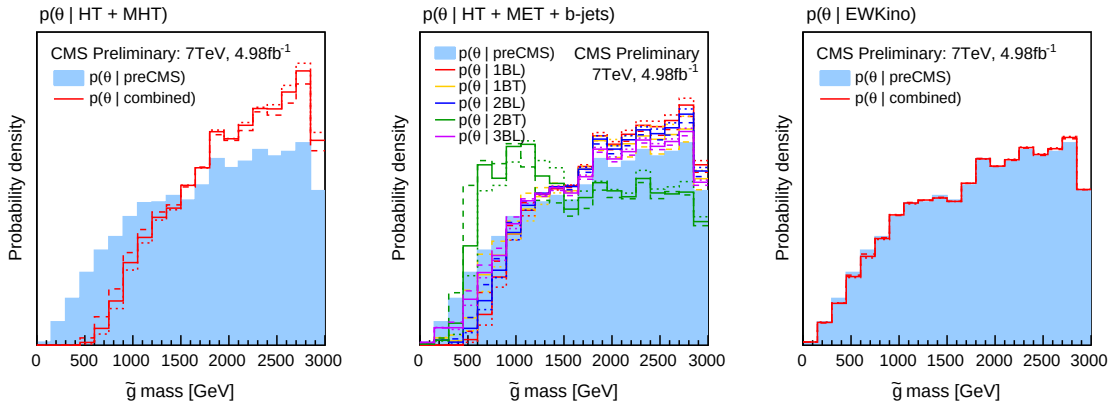

Figure 1: Marginalized 1D posterior probability distributions for $\tilde{g}$ mass. The line histograms in the three plots show posterior densities after including the three of the seven implemented CMS analyses: $H_T + H_T^{miss}$, $H_T + E_T^{miss} + b$-jets and EWKino. Within each analysis, different search regions are combined if they are exclusive, or shown separately otherwise. Solid curves show the posterior densities obtained from likelihoods calculated using the central values of estimated signal counts s, whereas the dashed and dotted lines show the posterior densities obtained from likelihoods calculated using $s - 0.5s$ and $s + 0.5s$ respectively.

Third generation squarks play a special role in the MSSM, and searches for light stops and sbottoms have become a high priority in the analyses of the 8 TeV data. The main interest is to address the question of naturalness in SUSY. In our sampled sub-space, the stop mass distribution is dominated by preCMS data (plus the Higgs mass constraint) and $m_{\tilde{t}_1}$ typically lies in the 1–2.5 TeV range, although values down to ~ 500 GeV are possible (the probability to have $m_{\tilde{t}_1} < 1$ TeV is 9.3% in our analysis). This is illustrated in the middle row of Fig. 2, which shows no visible effect from the CMS analyses. The situation is a bit different for the sbottoms (see the bottom row of Fig. 2): first, the preCMS distribution shows a considerable probability of 24.6% for $\tilde{b}_1$ masses below 1 TeV; second, the 2BT search prefers sbottoms of order 0.3–1 TeV.

[7]The analysis in Ref. [43] used two background estimates. In this study, we have used the E_T^{miss}-reweighting background estimate. The other estimate, referred to as the nominal estimate, yields a 1.1σ excess.

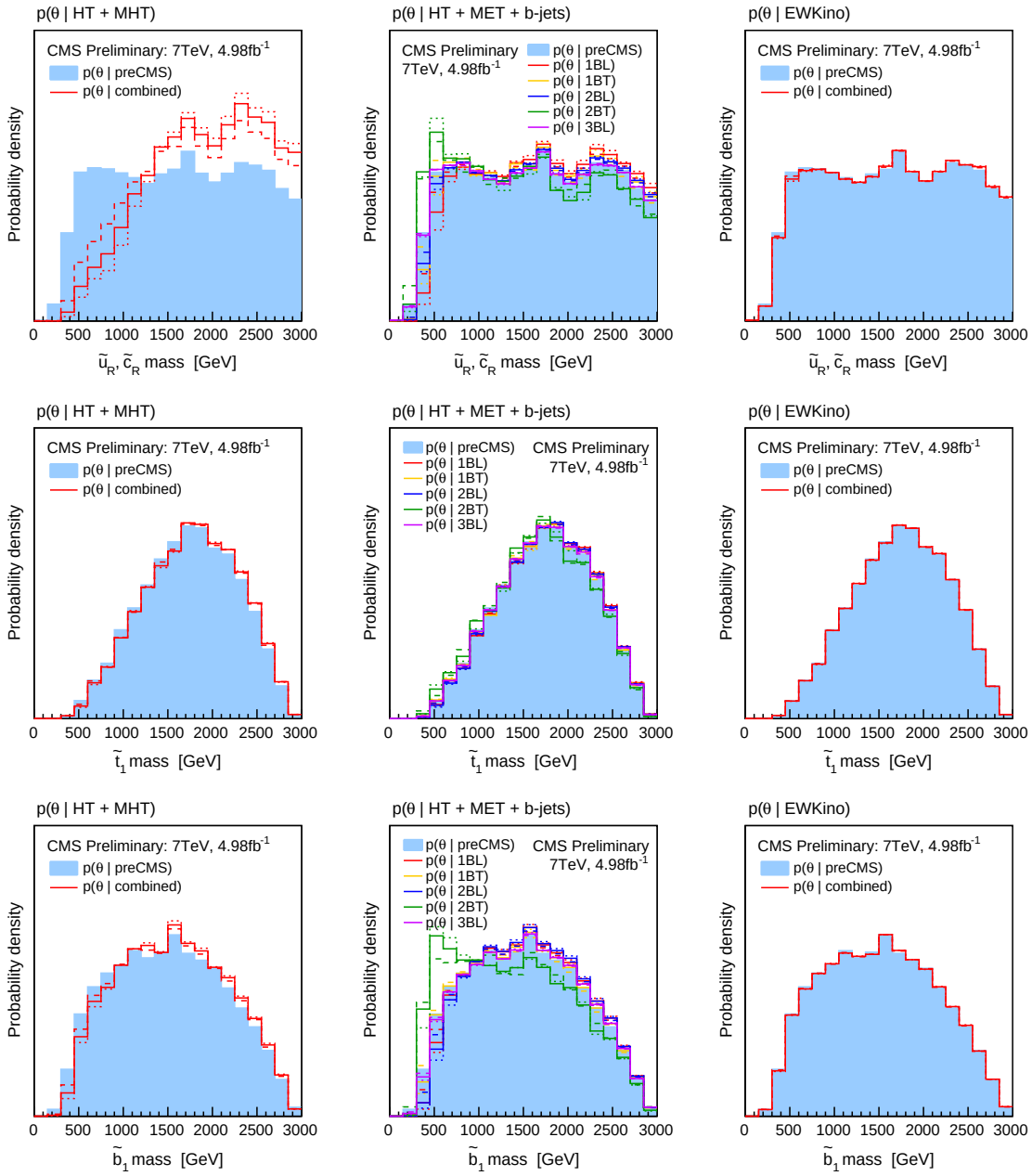

Figure 2: Marginalized 1D posterior probability distributions for $\tilde{u}_R$ mass, $\tilde{t}_1$ mass and $\tilde{b}_1$ mass. The filled blue histograms in each plot show the posterior densities after preCMS measurements. In each row, the line histograms in the three plots show posterior densities after including the three of the seven implemented CMS analyses: $H_T + H_T^{miss}$, $H_T + E_T^{miss} + b$-jets and EWKino. Within each analysis, different search regions are combined if they are exclusive, or shown separately otherwise. Solid curves show the posterior densities obtained from likelihoods calculated using the central values of estimated signal counts s, whereas the dashed and dotted lines show the posterior densities obtained from likelihoods calculated using $s - 0.5s$ and $s + 0.5s$ respectively.

Next, we turn to the $\tilde{\chi}_1^0$ mass distributions shown in the top row of Fig. 3. At the preCMS stage, $\tilde{\chi}_1^0$ masses are already limited to values below ∼1TeV because in this realization of the pMSSM the lightest neutralino is assumed to be the LSP. Including the CMS analyses, we observe that the $H_T + H_T^{miss}$ analysis again induces a noticeable shift towards higher masses whereas $H_T + E_T^{miss} + b$-jets leads to a shift to lower values. These shifts are primarily due to the associated shifts in the $\tilde{g}$ and $\tilde{u}_R$ masses discussed above. Note that although in the pMSSM (contrary to, e.g., the CMSSM) the neutralino, gluino, and squark masses can be varied independently of each other, the requirement of a neutralino LSP induces a slight correlation between the $\tilde{\chi}_1^0$ mass and the $\tilde{g}$ and $\tilde{u}_R$ masses: as the phase space for lighter gluinos and up squarks shrinks, heavier neutralinos become more probable, and vice versa. Moreover, for a given gluino or squark mass, events with lighter LSPs have more E_T^{miss}, and hence yield stronger constraints. The 2D probability distributions for the $\tilde{\chi}_1^0$ mass versus $\tilde{g}$ and $\tilde{u}_R$ masses are shown in Fig. 4, both before and after the inclusion of the CMS analyses.

The middle and bottom rows of Fig. 3 display the distributions for the $\tilde{\chi}_2^0$ and $\tilde{\chi}_1^\pm$ masses, which again show a tendency to be shifted to higher (lower) values by the $H_T + H_T^{miss}$ ($H_T + E_T^{miss} + b$-jets) results. These shifts are due to reasons similar to those described above for $\tilde{\chi}_1^0$. A particularity of the posterior distribution of the $\tilde{\chi}_1^\pm$ mass is that it peaks at low values around 300 GeV. This is a consequence of the Δa_μ constraint (see Table 1). Although we do not show here the posterior distribution of μ, we note that the preference for a light chargino goes hand in hand with a preference for small $|\mu|$, which is advantageous in view of the little hierarchy problem of SUSY. (Recall that $-m_Z^2/2 = \mu^2 + m_{H_u}^2$ with $m_{H_u}^2 \lesssim 0$ inducing EWSB. Therefore, to avoid large cancellations, $\mu \approx \mathcal{O}(m_Z)$ is preferred by naturalness arguments.) No significant variation is observed in the $\tilde{\chi}_{3,4}^0$ and $\tilde{\chi}_2^\pm$ masses.

The upper row of Fig. 5 shows the 2D distributions for $\tilde{\chi}_1^\pm$ mass versus $\tilde{\chi}_2^0$ mass. The lower row shows the $\tilde{\chi}_1^\pm$ mass versus the $\tilde{\chi}_1^0$ mass. The former shows that there are many points with a bino-like $\tilde{\chi}_1^0$ for which the $\tilde{\chi}_2^0$ and $\tilde{\chi}_1^\pm$ are quite close in mass. In fact, at the preCMS level the probabilities to have $(m_{\tilde{\chi}_1^\pm} - m_{\tilde{\chi}_2^0})/m_{\tilde{\chi}_1^\pm}$ less than 0.01 or 0.1 are 72.2% and 94.5%, respectively. The bottom row of Fig. 5 shows that there are also many points for which the $\tilde{\chi}_1^0$ is either wino-like or higgsino-like, in which case the $\tilde{\chi}_1^\pm$ is nearly degenerate with the $\tilde{\chi}_1^0$. The probabilities of having $(m_{\tilde{\chi}_1^\pm} - m_{\tilde{\chi}_1^0})/m_{\tilde{\chi}_1^\pm}$ to be less than 0.01 and 0.1 are 23.1% and 34.7% respectively. These results are, of course, those obtained including the $c\tau < 10$ mm cut. The influence and importance of this cut as well as the various different $\tilde{\chi}_1^0$ cases are discussed in Appendix A. Finally, comparing the left-hand plots of Fig. 5 to the right-hand plots makes it apparent that the CMS EWKino combined results have hardly any impact on the distributions of the above mass differences.

The effect of the CMS analyses on the total sparticle production cross section is shown in Fig. 6. The $H_T + H_T^{miss}$ search has a large effect on the cross section, reducing the most probable cross section values by more than an order of magnitude, from $\mathcal{O}$(50 fb) to $\mathcal{O}$(1 fb). The high cross sections, which are less favored, are due to light gluinos and squarks, which lead to dominant gluino and squark production. Of course, the $H_T + E_T^{miss} + b$-jets analysis yields a shift to higher cross section values. The relation between $\tilde{g}$ and $\tilde{u}_R$ masses and the cross section, as well as the influence of the CMS analyses on it, is shown in Fig. 7. The first point to note is that the total SUSY cross section is not a simple function of just one or two sparticle masses. Rather, the cross section can be large even when squarks and gluinos are heavy, e.g. due to large electroweak gaugino production. The second point to note is that for light squarks and gluinos the cross section is always very large. It is largely this tail of large cross section values for light squarks and gluinos that is limited by the CMS analyses (unless the mass splittings are very small, as

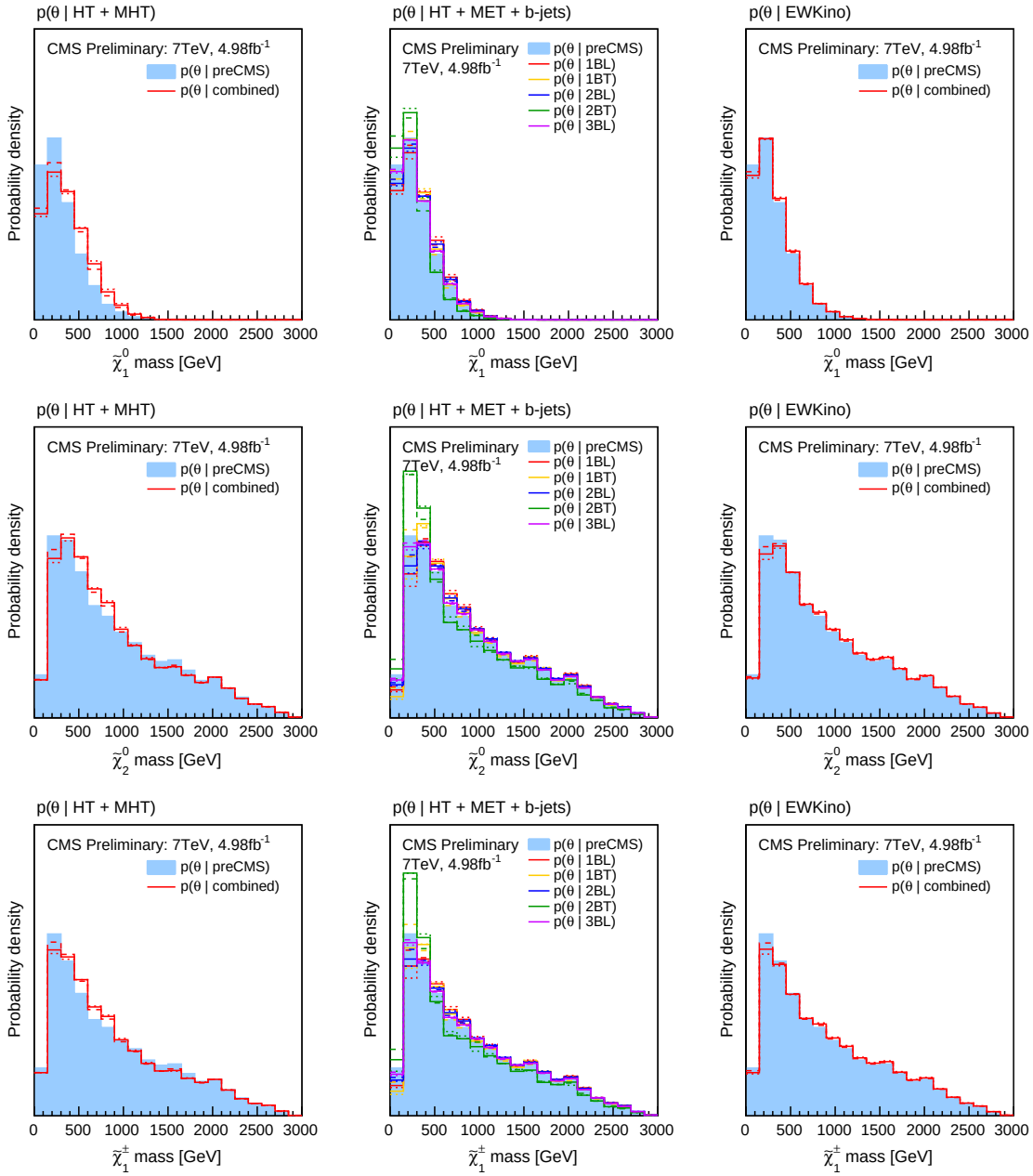

Figure 3: Marginalized 1D posterior probability distributions for $\tilde{\chi}_1^0$ mass, $\tilde{\chi}_2^0$ mass and $\tilde{\chi}_1^\pm$ mass. The filled blue histograms in each plot show the posterior densities after preCMS measurements. In each row, the line histograms in the three plots show posterior densities after including the three of the seven implemented CMS analyses: $H_T + H_T^{miss}$, $H_T + E_T^{miss} + b$-jets and EWKino. Within each analysis, different search regions are combined if they are exclusive, or shown separately otherwise. Solid curves show the posterior densities obtained from likelihoods calculated using the central values of estimated signal counts s, whereas the dashed and dotted lines show the posterior densities obtained from likelihoods calculated using $s - 0.5s$ and $s + 0.5s$ respectively.

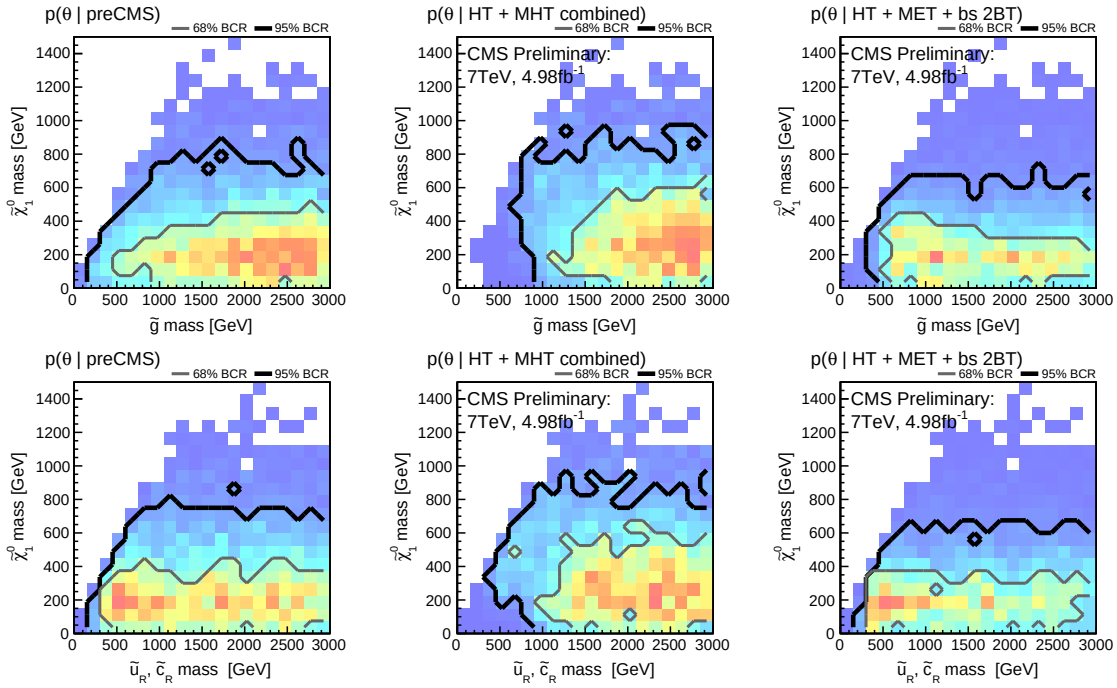

Figure 4: Marginalized 2D posterior probability distributions for $\tilde{\chi}_1^0$ mass versus $\tilde{g}$ mass and $\tilde{\chi}_1^0$ mass versus $\tilde{u}_R$ mass. In each row, the 1st plot shows the preCMS posterior density. The 2nd and 3rd plots show posterior densities after applying the $H_T + H_T^{miss}$ combined and $H_T + E_T^{miss} + b$-jets 2BT results respectively. The grey and black contours enclose the 68% and 95% Bayesian credible regions respectively.

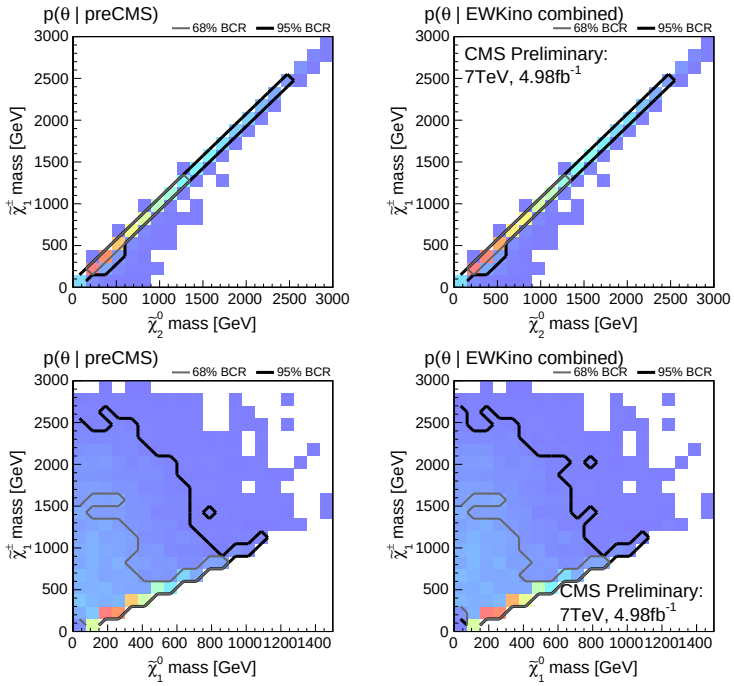

Figure 5: Marginalized 2D posterior probability distributions for $\tilde{\chi}_1^{\pm}$ mass versus $\tilde{\chi}_2^0$ mass and $\tilde{\chi}_1^{\pm}$ mass versus $\tilde{\chi}_1^0$ mass. In each row, the 1st plot shows the preCMS posterior density. The 2nd plot shows the posterior densities after applying the EWKino combined results. The grey and black contours enclose the 68% and 95% Bayesian credible regions respectively.

we shall see below).

In summary, the hadronic 2011 CMS analyses have a visible impact on the allowed values of some of the sparticle masses, especially on the masses of gluinos and light-flavor squarks. The leptonic analyses however do not have a visible effect, largely because the region of the pMSSM parameter space to which they could be sensitive is limited.

4.2 Current sensitivity to the pMSSM

Our results show that there are still many regions in the pMSSM parameter space to which current CMS searches are insensitive. It is necessary to find these regions, explore their topologies, and devise new searches for them if we wish to make a general statement about the viability of the pMSSM, and by association, the MSSM. In this section, we report the status of our exploration of these regions.

There are several reasons why current searches may be insensitive to some regions of the pMSSM. It could be that the signal cross sections are simply too low to be explored with the available integrated luminosities. Or it could be that the mass splittings between some SUSY particles are small, yielding jets and leptons of lower p_T on average than those that can be studied with current searches. Or, perhaps, the E_T^{miss} is lower on average than the E_T^{miss} thresholds in current analyses. But, before we can characterize these regions, which we shall refer to as *unexplored regions*, we need to define them using an appropriate criterion.

A search is insensitive to new physics if the analysis cannot distinguish between the background plus signal hypothesis, denoted by H_1, and the background-only hypothesis, denoted by H_0. In the current study, the likelihood for hypothesis H_1 at the point θ is given in Eq. (7),

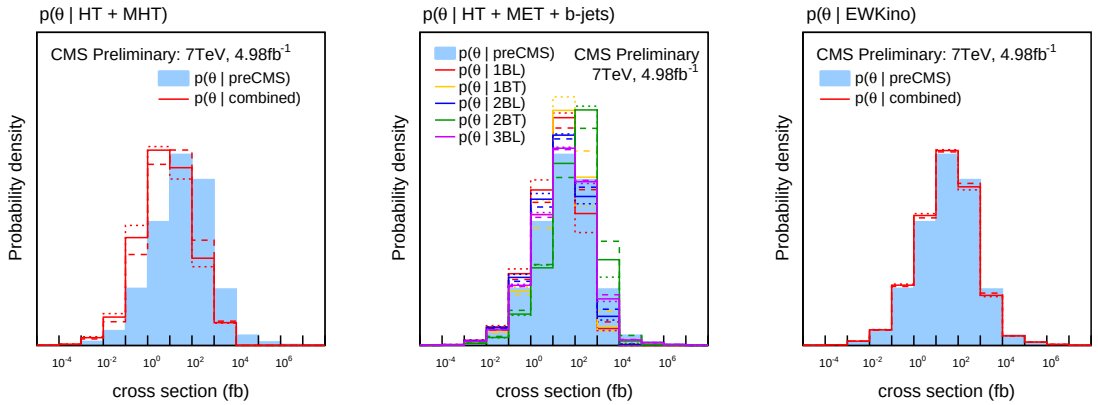

Figure 6: Marginalized 1D posterior probability distributions for the total sparticle production cross section. The filled blue histograms in each plot show the posterior densities after preCMS measurements. The line histograms in the three plots show posterior densities after including the three of the seven implemented CMS analyses: $H_T + H_T^{miss}$, $H_T + E_T^{miss} + b$-jets and EWKino. Within an analysis, different search regions are combined if they are exclusive, or shown separately otherwise. Solid curves show the posterior densities obtained from likelihoods calculated using the central values of estimated signal counts s, whereas the dashed and dotted lines show the posterior densities obtained from likelihoods calculated using $s - 0.5s$ and $s + 0.5s$ respectively.

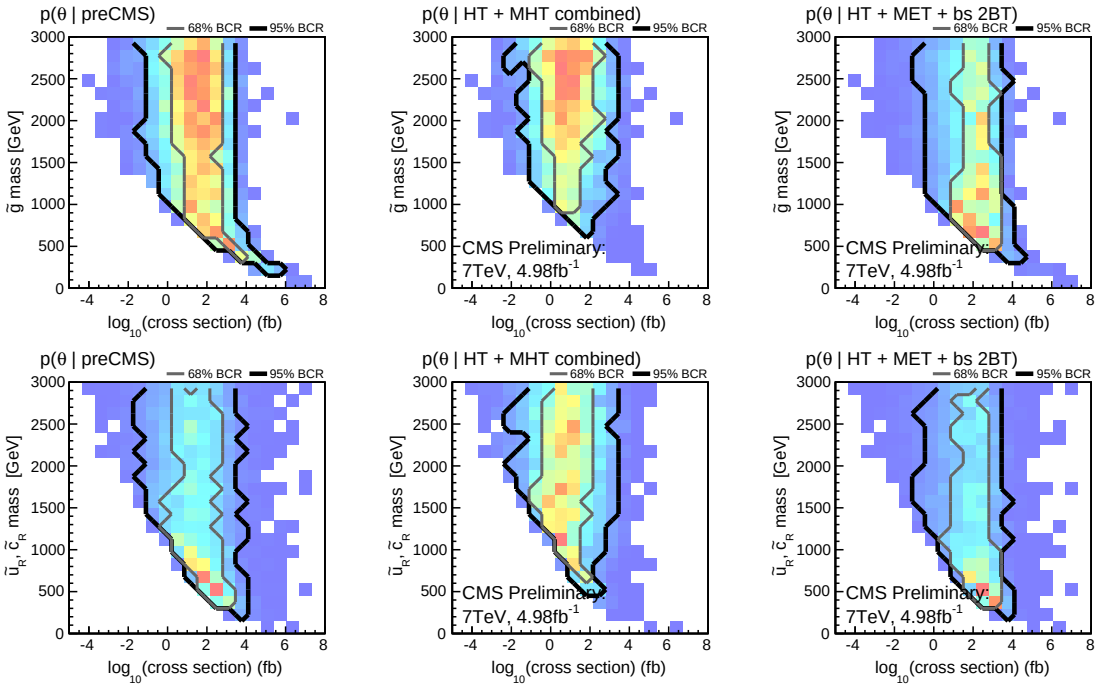

Figure 7: Marginalized 2D posterior probability distributions for $\tilde{g}$ mass versus log total sparticle production cross section and $\tilde{u}_R$ mass versus log total sparticle production cross section. In each row, the 1st plot shows the preCMS posterior density. The 2nd and 3rd plots show posterior densities after applying the $H_T + H_T^{miss}$ combined and $H_T + E_T^{miss} + b$-jets 2BT results respectively. The grey and black contours enclose the 68% and 95% Bayesian credible regions respectively.

while the likelihood for H_0 is given by the same equation, but with $s_l = 0$. For clarity, we use a slightly more precise notation and write the first likelihood, $L(D^{\rm CMS}|\theta)$, as $L(D^{\rm CMS}|\theta, H_1)$ and the background-only likelihood as $L(D^{\rm CMS}|H_0)$. We use the *local*[8] Bayes factor[9]

$$B_{10}(\theta) = L(D^{\rm CMS}|\theta, H_1)/L(D^{\rm CMS}|H_0), \tag{8}$$

as a measure of the relative probabilities of the two hypotheses H_1 at θ and H_0.

It is convenient to map the Bayes factor to the scale defined by the transformation

$$Z = \text{sign}(\ln \text{B}_{10})\sqrt{2|\ln \text{B}_{10}|}, \tag{9}$$

which is a signed Bayesian analog of the frequentist "n-sigma". In conventional language, the case $B_{10}(\theta) \gg 1$ would indicate a signal at "Z-sigma significance", while the case $1/B_{10}(\theta) \gg 1$ would indicate a signal *exclusion* at "Z-sigma significance". Note that in our definition of Z, negative values correspond to exclusions while positive values are associated with potential observations. A search is insensitive if $B_{10}(\theta) \sim 1$, that is, if $Z \sim 0$. However, in order to have well-defined boundaries for the unexplored regions, we shall require that the points within them satisfy

$$|Z| \leq 2. \tag{10}$$

A point with $Z > 5$ would signify a discovery while $Z < -1.64$ would mean that the point is excluded at 95% confidence level (CL).

We can calculate an overall significance for a set of analyses using the combined likelihoods, if the analyses are exclusive. The Bayes factor in this case will be given by

$$B_{10}(\theta) = \frac{\prod_l L(D_l^{\rm CMS}|\theta, (H_1)_l)}{\prod_l L(D_l^{\rm CMS}|(H_0)_l)}. \tag{11}$$

In this study, we have used the above combined likelihoods for combining the exclusive search regions within a given analysis. However the various analyses, and sometimes even the search regions within a single analysis considered here are sometimes not exclusive. In this case we simply take the best significance, which we define as the significance Z with the largest absolute value, that is,

$$\begin{aligned} l_{best} &\equiv \arg\max_l(|Z_l|), \\ Z_{best} &= Z_{l_{best}}, \end{aligned} \tag{12}$$

where l_{best} is the index of the analysis with the largest absolute significance. Whenever there is a combined likelihood available for an analysis, as in $H_T + H_T^{miss}$, OS 2ℓ and EWKino analyses, we include the single Z value obtained from that likelkhood into the Z_{best} calculation. Whenever a combined likelihood cannot be obtained from the search regions in an analysis, as in $H_T + E_T^{miss} + b$-jets, $H_T + E_T^{miss} + \tau$s, monojet $+E_T^{miss}$ or SS 2ℓ analyses, we include the Z value from each search region in the Z_{best} calculation.

[8] We refer to this as the local Bayes factor to distinguish it from the *global* Bayes factor $B_{10} = L(D^{\rm CMS}|H_1)/L(D^{\rm CMS}|H_0)$, in which the likelihood $L(D^{\rm CMS}|\theta, H_1)$ times the prior $p(\theta|H_1) = p(\theta)$ is marginalized with respect to θ. Note, for this operation to yield an unambiguous (global) Bayes factor the prior must be proper, that is, $\int p(\theta|H_1)\, d\theta = 1$.

[9] This is a Bayes factor rather than a likelihood ratio because the likelihoods have been marginalized (see Eq. (6)) with respect to some of the model parameters, here the expected backgrounds.

In Fig. 8, we plot the marginalized 1D posterior densities of the best significance Z_{best}. The left histogram depicts the preCMS distribution of this quantity, that is, the best significance distribution incorporating preCMS likelihoods only. About 32% of the pMSSM points we analyze have cross sections smaller than 10 fb. About 63% of the points in the left plot have $|Z_{best}| < 2$, and hence are inaccessible with 5 fb^{-1} of 7 TeV LHC data. The right plot of Fig. 8 shows the best significance distribution for points with cross section greater than 10 fb, which are much more likely to be accessible with 5fb^{-1} of 7 TeV LHC data. The probability of having $|Z_{best}| < 2$ in this case is 45%. As expected, the best significance distribution is wider, and the impact of the CMS analyses in this accessible subset of the pMSSM sub-space is much greater.

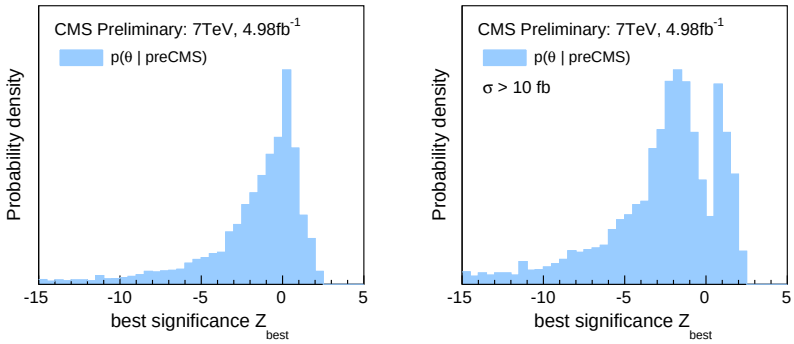

Figure 8: Marginalized 1D posterior distributions for the best significance Z_{best} weighted according to preCMS likelihood without and with a lower limit on the production cross section of $\sigma > 10$ fb. As expected, the lower bound on the cross section pushes the distribution towards pMSSM points that would be decisively excluded by the CMS analyses.

The $|Z_{best}|$ value can be used to construct a binary likelihood of the combination of all analyses where $p(|Z_{best}| < 2|\theta) = 1$ and $p(|Z_{best}| \geq 2|\theta) = 0$. The distributions of points with $|Z_{best}| < 2$ can be viewed as the probability densities of the so-called *non-excluded points*, that is, points that lie in the region we have called unexplored. Figure 9 shows the marginalized 1D posterior densities for the points with $|Z_{best}| < 2$ compared with the preCMS distributions for selected sparticle masses and the total sparticle production cross section. Again we see that the CMS analyses have the most impact on $\tilde{g}$ and light-flavor squark masses and cross section. This is followed by the 3rd generation squarks and EW gauginos. Comparing these distributions with those in Figs. 1–6, we see that $H_T + H_T^{miss}$ results are more decisive compared to jets + $E_T^{miss} + b$-jets in our rough combination, implying that the posterior densities for the masses of the above particles are shifted to higher values relative to the preCMS density.

We have also extensively explored the consequences of the results included in our study on the Higgs bosons of the MSSM, in particular, on the distributions of production/decay rates of the MSSM Higgses compared to the SM Higgs boson. Our results can be found in Appendix E. Furthermore, in Appendix F, we show the impact of the CMS results on dark matter-related observables such as the relic density, spin-independent and spin-dependent dark matter detection cross sections. The influence of CMS results is characterized by examining the extent to which the $|Z_{best}| < 2$ requirement impacts preCMS distributions. In the case of Higgs bosons, Appendix E shows that for the most part, this impact is very small and expectations for the Higgs bosons are dominated by the preCMS constraints. With regard to dark matter, Appendix F shows that the $|Z_{best}| < 2$ CMS result increases the probability for $\Omega_{\tilde{\chi}_1^0} \sim 0.01$ vs. $\Omega_{\tilde{\chi}_1^0} \sim 1$, but does not increase the probability to be in the WMAP window near $\Omega_{\tilde{\chi}_1^0} \sim 0.1$. However, the 95% credible region for $\Omega_{\tilde{\chi}_1^0} \sim 0.1$ is shifted to somewhat higher $m_{\tilde{\chi}_1^0}$ values.

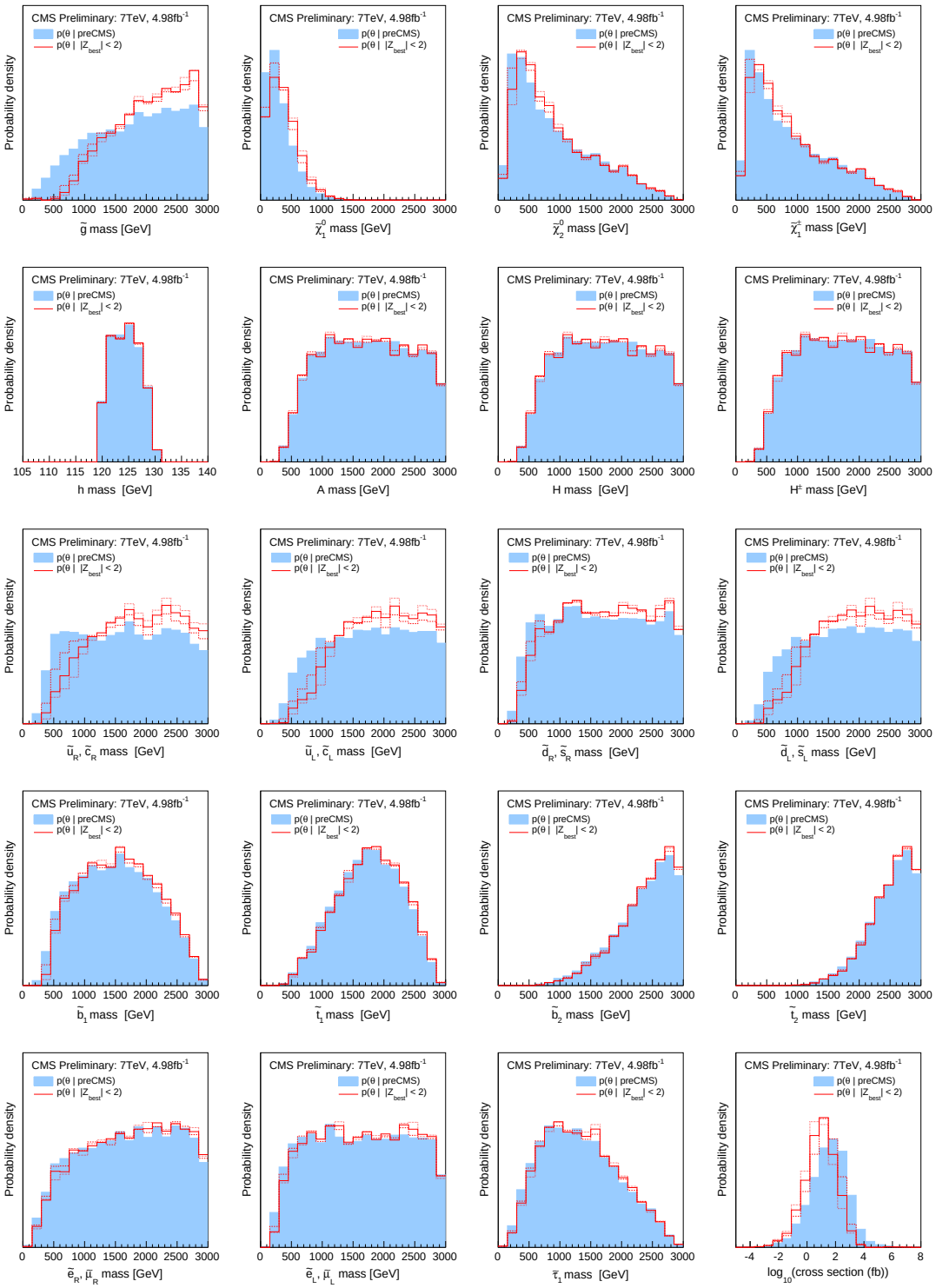

Figure 9: Marginalized 1D posterior densities for selected sparticle masses and total sparticle production cross section. The filled blue histograms in each plot show the posterior densities after preCMS measurements. The line histograms show the normalized distributions of points that have best significance $|Z_{best}| < 2$, i.e., points that are not excluded. The solid curves show the distributions obtained from likelihoods (and significances) calculated using the central values of estimated signal counts s, while the dashed and dotted lines show the distributions obtained from likelihoods (and significances) calculated using $s - 0.5s$ and $s + 0.5s$, respectively.

We conclude this section by reiterating one of the primary aims of this work, namely, to find the parameter regions and signatures to which the CMS searches are insensitive and to guide the design of dedicated analyses that would target such signatures. To that end, we performed an extensive study that characterized the unexplored regions with the help of Simplified Models. The results of this study can be found in Appendix G.

5 Conclusions

We have investigated the impact of a subset of the 7 TeV CMS SUSY searches on a potentially accessible sub-space of the pMSSM, a 19-dimensional proxy of the MSSM defined at the SUSY scale. By construction, the pMSSM explicitly avoids GUT scale assumptions. What may or may not happen at the GUT scale is an interesting theoretical question that is not our focus.

A 19-dimensional sub-space of the pMSSM has been sampled using an MCMC method and a posterior density — subsequently used as the prior in the interpretation of the CMS results — that is proportional to a likelihood function, constructed from a variety of pre-CMS results, times a flat "ur-prior", that is, a prior that starts the chain of inference. Because the ur-prior is chosen to be flat, the sampled points also constitute a discrete approximation to the pre-CMS likelihood to which, in principle, likelihood methods could be applied. However, we have pursued a Bayesian approach. The sub-space has been chosen to cover sparticle masses up to about 3 TeV. The seven analyses implemented span a variety of final states, which, in principle, permit a broad exploration of the pMSSM and by association the MSSM.

The hadronic search $H_T + H_T^{miss}$ followed by the hadronic searches $H_T + E_T^{miss} + b$-jets and monojet $+E_T^{miss}$ are found to be the most decisive in constraining the pMSSM, while the hadronic search $H_T + E_T^{miss} + \tau$s and leptonic searches SS 2ℓ, OS 2ℓ and EWKino, based on 5 fb^{-1} of 7 TeV data, have much less visible impact, with the EWKino analysis being the most sensitive among the leptonic analyses. We find some tension between the hadronic analyses in that the first favors high $\tilde{g}$ mass, while the second ($H_T + E_T^{miss} + b$-jets) prefers low masses. This is due to the 2.2σ excess over background observed in the 2 b-jet final state (in the 2011 data set) when the E_T^{miss}-reweighting background estimate is used [43]. The results of the CMS analyses favor higher mass for the squarks $\tilde{u}_{R,L}$ and $\tilde{d}_{R,L}$, stops with mass in the 1–2 TeV range, and sbottoms with mass below 1 TeV. Our overall conclusion is that the hadronic 2011 CMS analyses have a significant impact on the allowed values of the gluino and light-flavor squark masses, but third-generation squarks are much less affected. In particular, there is no visible effect on the stop mass distributions. (The change in sbottom mass distribution is caused by the small excess in the $H_T + E_T^{miss} + b$-jets analysis.) We also see a slight limiting of the LSP mass distribution. The leptonic analyses, however, do not have a noticeable effect, largely because the region of the pMSSM parameter space to which they could be sensitive is limited. In particular, The EWKino searches, so far, have only a marginal effect on the neutralino and chargino mass distributions.

We have conducted a preliminary exploration of pMSSM points that escaped scrutiny by current searches, points we refer to as "unexplored". Of the 7205 model points explored, the seven analyses included in this study excluded 2701, or 37%. A preliminary exploration of the remaining 4504 model points indicates that 2198, or 49% of them have a total cross section > 10 fb, and thus according to the pMSSM would produce sufficient numbers of sparticle pairs that one might expect sensitivity to their existence using the 7 TeV CMS data set. Among these high cross section model points, 1188 (757) are dominated by electroweak (strong) production of charginos and neutralinos (squark pairs, including sbottom pairs). The dominant decay phenomenology for 803 of the 1188 weakino model points is production of a pair of charginos or

neutralinos almost degenerate ($\Delta(\text{EWK}) < 5$ GeV, see Eq. 20) in mass with the LSP, leading to little or no visible energy from their decay. The unexplored points with large cross section for the production of gluinos and, or, squarks are typified by scenarios in which there is significant degeneracy between the gluino/squark masses and the charginos/neutralinos, so-called "compressed spectra". The exploration of both kinds of unexplored points will benefit from "monojet" analyses in which initial state radiation supplies the monojet and the recoiling supersymmetric particles are too closely clustered in mass to give a significant number of energetic leptons or jets or a significant amount of missing energy.

This study, the first of its kind in CMS, demonstrates that a rigorous approach to testing the general MSSM, without theoretical prejudices on the patterns of SUSY soft-breaking terms, is absolutely feasible. The study indicated that close to 40% of the pMSSM sub-space below 3 TeV, for the non-degenerate chargino-neutralino case, is now ruled out. However, this study also showed that the analyses of the existing data have not dramatically changed the posterior distributions of most of the sparticle masses. Moreover, we have found unexplored regions of the pMSSM sub-space with cross sections that are sufficiently large as to suggest they should be accessible by the LHC, but are currently not constrained by virtue of significant degeneracy among the sparticles. Such degeneracies are allowed in the pMSSM as well as in GUT scale models that go beyond the CMSSM. It seems clear that if we are to maximize the potential of the LHC to explore SUSY in its full diversity, we need to develop a systematic approach to analysis construction that includes maximizing sensitivity to models and parameter choices that render the discovery SUSY particularly challenging. The current study provides an initial set of directions for this exploration.

This wide-ranging study has generated a vast treasure trove of information. For the interested reader, a subset of this information is provided in the appendices.

A Chargino–neutralino mass degeneracy in pMSSM

When freely scanning over the neutralino and chargino mass parameters M_1, M_2 and μ, we are very likely to find configurations which lead to degenerate or almost degenerate masses for the $\tilde{\chi}_1^0$ and $\tilde{\chi}_1^\pm$ (and $\tilde{\chi}_2^0$). In the convention where $M_1, M_2 > 0$, such degeneracy arises when either M_2 or $|\mu|$ is the smallest mass parameter, with the others being significantly larger. The former condition leads to a degenerate pair of wino-like $\tilde{\chi}_1^0$ and $\tilde{\chi}_1^\pm$, the latter to a triplet of (somewhat less) degenerate higgsino-like $\tilde{\chi}_{1,2}^0$ and $\tilde{\chi}_1^\pm$.

The leading and next-to-leading terms in the expressions for the neutralino and chargino masses in the MSSM were worked out in [38]. The occurrence of the degeneracies can be understood from the approximate expressions for the mostly bino, wino and higgsino-like neutralinos (see Eqs. (40)–(43) [38]):

$$M_{\tilde{B}} \simeq M_1 + \frac{m_Z^2(M_1 + \mu \sin 2\beta)\sin^2\theta_W}{M_1^2 - \mu^2} \tag{13}$$

$$M_{\tilde{W}} \simeq M_2 + \frac{m_Z^2(M_2 + \mu \sin 2\beta)\cos^2\theta_W}{M_2^2 - \mu^2} \tag{14}$$

$$M_{\tilde{H}_1^0} \simeq |\mu| + \frac{m_Z^2(1 - \sin 2\beta)(\mu + M_2 \sin^2\theta_W + M_1 \cos^2\theta_W)\mathrm{sgn}(\mu)}{2(\mu + M_2)(\mu + M_1)} \tag{15}$$

$$M_{\tilde{H}_2^0} \simeq |\mu| + \frac{m_Z^2(1 + \sin 2\beta)(\mu - M_2 \sin^2\theta_W - M_1 \cos^2\theta_W)\mathrm{sgn}(\mu)}{2(\mu - M_2)(\mu - M_1)} \tag{16}$$

and for the mostly wino and mostly higgsino-like charginos (see Eqs. (36) and (37) of [38]):

$$M_{\tilde{W}^\pm} \simeq M_2 + m_W^2 \left[\frac{M_2 + \mu \sin 2\beta}{M_2^2 - \mu^2}\right] \tag{17}$$

$$M_{\tilde{H}^\pm} \simeq |\mu| + m_W^2 \mathrm{sgn}(\mu) \left[\frac{\mu + M_2 \sin 2\beta}{\mu^2 - M_2^2}\right] \tag{18}$$

If $|M_2\mu| < m_W^2 \sin 2\beta$ then replace $\mathrm{sgn}(\mu)$ with -1 above.

We see that the mass ordering depends upon the relative sizes of M_2 and $|\mu|$ in the case of the charginos and on the relative sizes of M_1, M_2, $|\mu|$ in the neutralino case. See Fig. 10 for illustration. Concretely, we observe:

1. The LSP (χ_1^0) mass is always determined by the smallest of $|\mu|$, M_2, and M_1 (and is higgsino, wino or bino in the 3 respective cases)
2. The $\chi_1^\pm$ mass is basically determined by the smallest of $|\mu|$ and M_2 (and is higgsino or wino in the two respective cases).
3. As shown in Fig. 11, in either the higgsino ($|\mu| < M_2, M_1$) or wino ($M_2 < |\mu|, M_1$) cases for the LSP, the chargino is automatically more or less degenerate in mass with the LSP.

A further important point concerns the magnitude of the corrections to the leading terms in the mass equations. Relative to the leading terms, the corrections are always of order $m_W^2/|\mu|^2$ or m_W^2/M_2^2 in the chargino case and of order $m_Z^2/|\mu|^2$ or m_Z^2/M_2^2 or m_Z^2/M_1^2 in the neutralino case. They are thus small factors times the leading terms of order $|\mu|$ or M_2 or M_1, since we are

typically operating in a region of parameter space where $|\mu|, M_{1,2} > 120$ GeV (LEP chargino limits). This implies that these corrections are typically small, and the mass eigenstates are indeed mostly bino-, wino- and higgsino-like, unless $M_2 \sim |\mu|$ (chargino and neutralino cases) or $M_1 \sim |\mu|$ or $M_1 \sim M_2$ (neutralino case, depending on $\mathrm{sgn}(\mu)$). Such cases are rare in the flat scans that we employ.

Focusing on Fig. 11, one sees that in the case where M_2 is the smallest mass parameter, $m_{\widetilde{\chi}_1^\pm} - m_{\widetilde{\chi}_1^0}$ is very small, typically below 500 MeV. This is to be expected from Eqs. (14) and (17) according to which $m_{\widetilde{\chi}_1^\pm} - m_{\widetilde{\chi}_1^0}$ is exactly zero to the order of the expansion done in the small M_2 case (for which $\widetilde{\chi}_1^0 \sim \tilde{W}^0$). In contrast, when $|\mu|$ is the smallest parameter, the mass differences are approximately given by $M_{\tilde{H}_1^\pm} - M_{\tilde{H}_1^0}$ and $M_{\tilde{H}_1^\pm} - M_{\tilde{H}_2^0}$, neither of which is exactly zero using the expansion formulae given above. Thus, in this case we expect $m_{\widetilde{\chi}_1^\pm} - m_{\widetilde{\chi}_1^0}$ to be much larger than in the small M_2 case and this is what we find numerically: for the higgsino-LSP case the mass difference is of order of a GeV or somewhat larger.

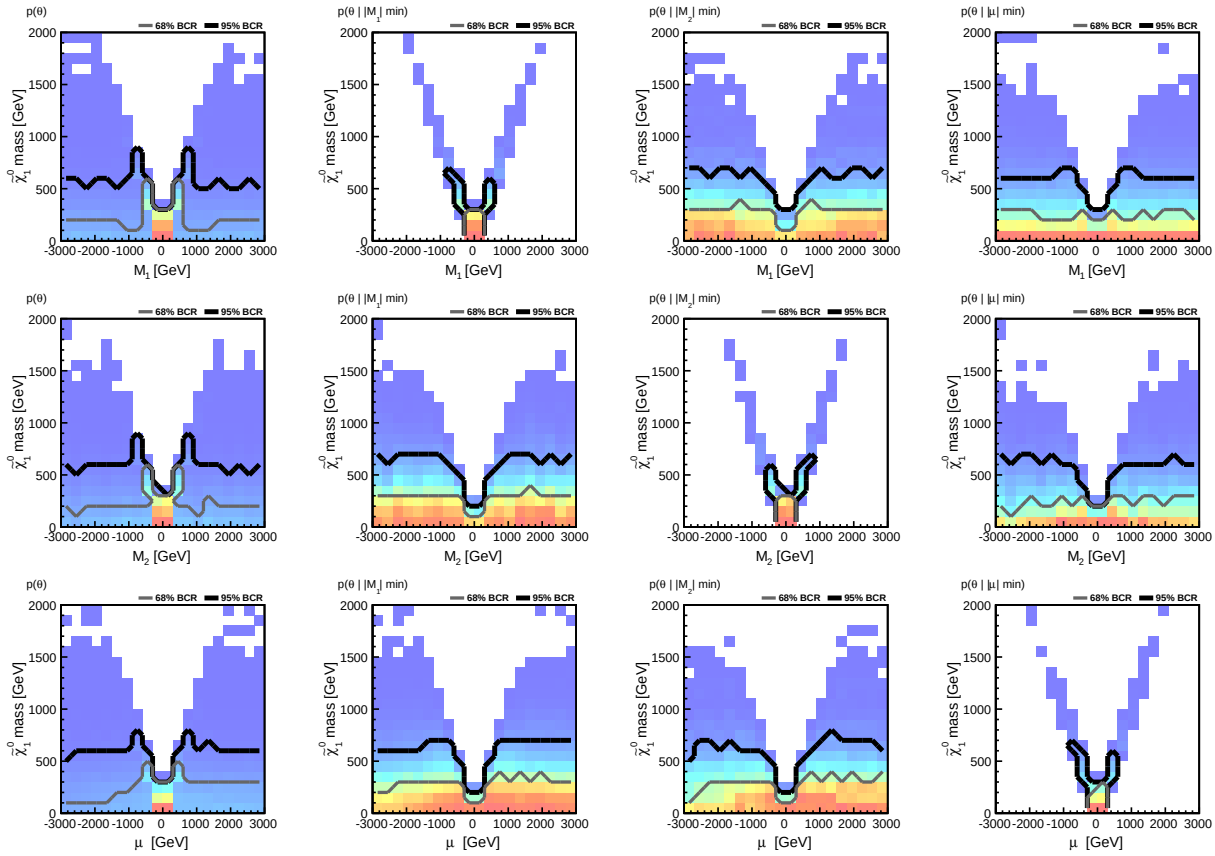

Figure 10: LSP mass versus M_1, M_2 and μ for the prior $p(\theta)$ obtained by a random scan of the pMSSM parameter space. Distributions are shown for all parameter configurations (1st column), for $|M_1|$ smallest (2nd column), for $|M_2|$ smallest (3rd column) and for $|\mu|$ smallest (4th column).

The plots of Fig. 5 provide a useful summary and can be used to explain the impact of the $c\tau < 10$ mm cut on pMSSM parameter space. The upper plots show the 2D distributions for $\tilde{\chi}_1^\pm$ mass versus $\tilde{\chi}_2^0$ mass while the lower plots show distributions for $\tilde{\chi}_1^\pm$ mass versus $\tilde{\chi}_1^0$ mass. From the upper plots, we see that the $\tilde{\chi}_2^0$ and the $\tilde{\chi}_1^\pm$ are frequently quite close in mass. As noted previously, at the preCMS level the probabilities to have $|m_{\tilde{\chi}_1^\pm} - m_{\tilde{\chi}_2^0}|/m_{\tilde{\chi}_1^\pm}$ less than 0.01 or 0.1

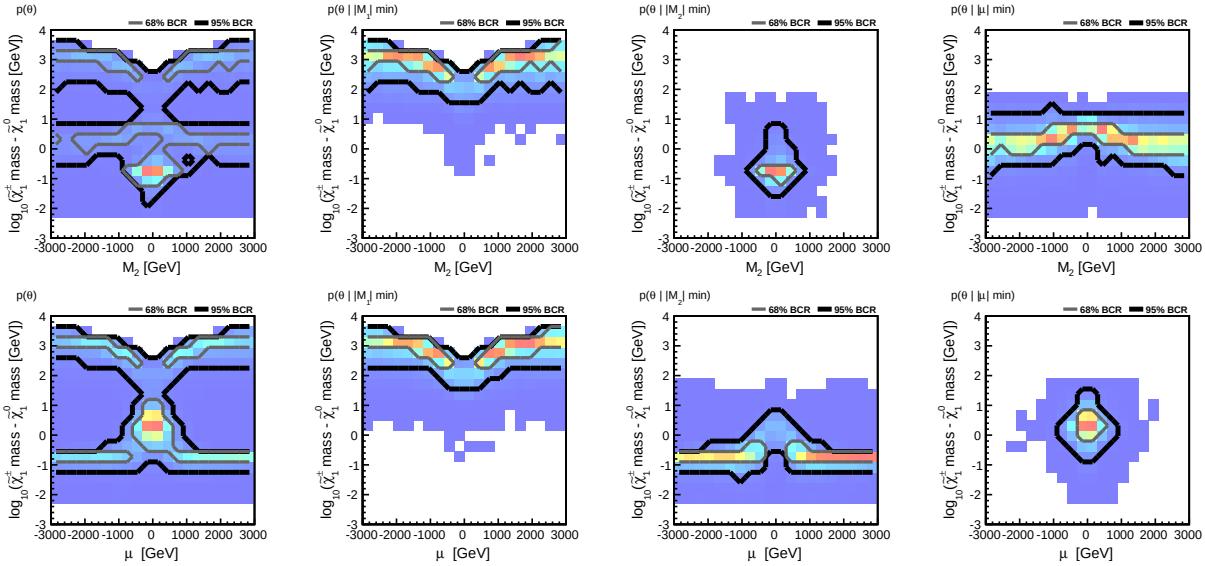

Figure 11: $\tilde{\chi}_1^\pm$ - $\tilde{\chi}_1^0$ mass difference versus M_2 and μ for the prior $p(\theta)$ obtained by a random scan of the pMSSM parameter space. Distributions are shown for all parameter configurations (1st column), for $|M_1|$ smallest (2nd column), for $|M_2|$ smallest (3rd column) and for $|\mu|$ smallest (4th column).

are 72.2% and 94.5%, respectively. Such a small mass difference is always present for the bino-like cases and is highly probable for the higgsino-like cases. In contrast, as noted above, large values of $|m_{\tilde{\chi}_1^\pm} - m_{\tilde{\chi}_2^0}|/m_{\tilde{\chi}_1^\pm}$ are typical of the wino-like cases. Instead, it is $(m_{\tilde{\chi}_1^\pm} - m_{\tilde{\chi}_1^0})$ that is always very small, in fact so small that there is a large probability that a wino-like case does not pass the $c\tau < 10$ mm cut. In comparison, only about 4% of the higgsino-like points (defined as those with $|\mu| < |M_2|, |M_1|$) are eliminated by the $c\tau$ cut. As a result of wino-like cases being eliminated by the $c\tau$ cut, the above probabilities would be smaller without the $c\tau < 10$ mm cut for the $\tilde{\chi}_1^\pm$ imposed in this study. Indeed, if we impose all the preCMS requirements except for the $c\tau$ cut, the above percentages become 53% and 69.4%. Still, despite the $c\tau$ cut, a significant number of pMSSM points with a wino-like LSP *are* retained and nearly all the higgsino-like points are retained. Both scenarios are characterized by small $(m_{\tilde{\chi}_1^\pm} - m_{\tilde{\chi}_1^0})/m_{\tilde{\chi}_1^\pm}$. Overall, with the $c\tau$ cut imposed, the probabilities of having $(m_{\tilde{\chi}_1^\pm} - m_{\tilde{\chi}_1^0})/m_{\tilde{\chi}_1^\pm}$ to be less than 0.01 and 0.1 are 23.1% and 34.7% respectively. These probabilities would be 43.8% and 52.3% if we imposed preCMS cuts without the $c\tau$ cut.

B PreCMS distributions of pMSSM parameters and masses

Figures 12 and 13 show the sampled distributions of selected parameters and masses and the effect of the model prior. The yellow filled histograms show the distributions associated with the pMSSM prior $p(\theta)$. All subsequent distributions (those indicated by line histograms) include the prompt chargino requirement, which affects the parameters M_1, M_2, and μ and the chargino and neutralino masses. As can be seen, the prompt chargino requirement has a dramatic influence on some distribution (for example M_2 and μ, and to a lesser extent M_1), but very little impact on the other parameters, for example, $\tan\beta$ and $m_{\tilde{Q}_3}$.[10] In all the plots, we

[10] A comment is in order regarding the difference between the $m_{\tilde{Q}_1}$ and $m_{\tilde{Q}_3}$ distributions at the $p_0(\theta)$ prior level. In fact the lower end of the $m_{\tilde{Q}_3}$ distribution is correlated with the A_t distribution: when $|A_t|$ is large, $m_{\tilde{Q}_3}$ (and

observe that the preCMS measurements incorporated in the MCMC influence the probability distributions relative to the simple prompt-chargino-decay distributions quite significantly, in particular shifting the gluino, squark, LSP and chargino masses to higher values, see Fig. 13. Also the stop mass distribution is shifted to higher values.

Imposing in addition 120 GeV $\leq m_h \leq$ 130 GeV strongly affects the distributions of A_t and the stop mixing parameter $X_t \equiv (A_t - \mu/\tan\beta)/\sqrt{m_{\tilde{t}_1} m_{\tilde{t}_2}}$; both distributions take on a two-peak structure emphasizing higher absolute values. This Higgs mass requirement also results in a slight shift of the $\tilde{t}_1$ mass distribution to somewhat larger values, compared to the preCMS constrains the effect is however quite small. Also shown is the effect of imposing the stricter requirement 123 GeV $\leq m_h \leq$ 128 GeV on the mass of the light Higgs boson (instead of $m_h \in [120, 130]$ GeV, as in Table 1). As expected, the only affected parameters are A_t and X_t, both of which shift to larger absolute values (on average) in order for the MSSM to yield a Higgs mass near 125 GeV. Note, in particular, that X_t values approaching maximal mixing are preferred, while the $m_{\tilde{t}_1}$ distribution basically remains unaffected. We conclude that the precise implementation of the recent Higgs mass measurement is not important for our analysis.

For completeness, Figs. 12 and 13 also show the impact of a requirement on the relic density of the LSP, taking either $\Omega_{\tilde{\chi}_1^0} h^2 < 0.136$ at 95% CL or $\Omega_{\tilde{\chi}_1^0} h^2 = 0.1123 \pm 0.0035_{\text{obs}} \pm 0.01123_{\text{theory}}$. As can be seen, such a requirement has a major impact on the LSP mass distribution, as well as on the LSP bino–wino–higgsino composition, and consequently on all other masses. (The peak for LSP masses of order 1 TeV arises because for a pure wino or pure higgsino LSP, the annihilation cross section is so high that the LSP has to be heavy, namely of order 1 TeV, to achieve $\Omega h^2 \sim 0.1$.) However, given the sensitivity of dark matter constraints to cosmological and astrophysical assumptions, we prefer not to use these constraints in constructing our model prior. Instead, we regard the properties of the LSP as a dark matter candidate an *output* of our analysis and discuss in Section F the consequences, if any, of LHC measurements for dark matter searches.

$m_{\tilde{U}_3}$) cannot be small, as this quickly leads to tachyonic stops. This mixing effect, which lowers one mass eigenstate, is not present for the first two generations. In turn, when $|A_t|$ is limited to be small, the $m_{\tilde{Q}_3}$ distribution becomes similar to the $m_{\tilde{Q}_1}$ distribution. At the $p(\theta|\text{preCMS})$ level, the $b \to s\gamma$ constraint in particular drives the stop mass parameters to higher values.

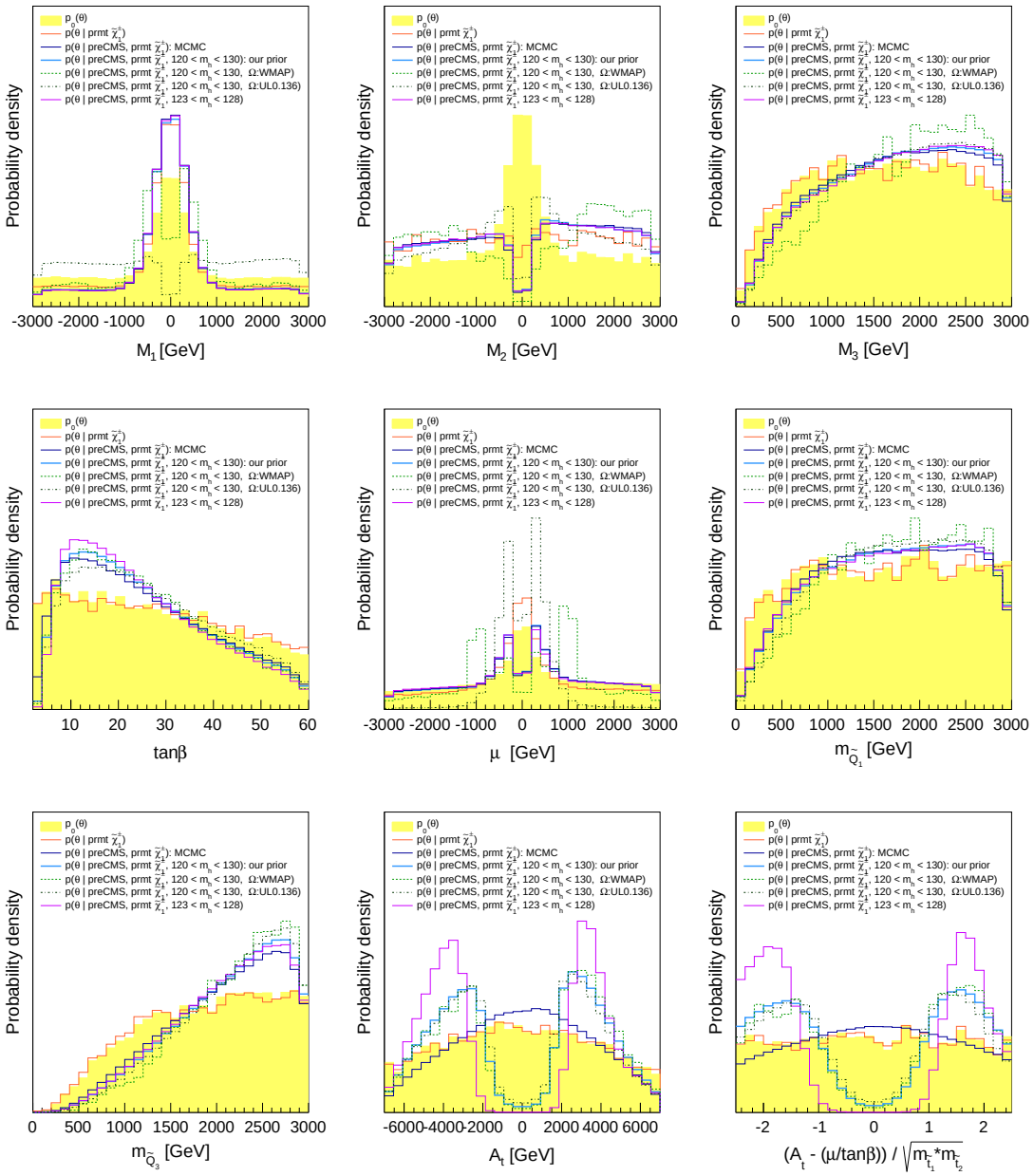

Figure 12: Marginalized 1D posterior densities for various pMSSM model parameters based on the "preCMS" measurements of Table 1 and various constraints on prompt charginos (prmt), the mass, m_h, of the light neutral Higgs boson, h, and LSP relic density $\Omega_{\tilde{\chi}_1^0}h^2$ (UL0.136: $\Omega_{\tilde{\chi}_1^0}h^2 < 0.136$, WMAP: $\Omega_{\tilde{\chi}_1^0}h^2 = 0.1123 \pm 0.0035_{\text{obs}} \pm 0.01123_{\text{theory}}$). The yellow histograms show the sampled distributions with a flat prior. The last plot shows that large values of $X_t = (A_t - \mu/\tan\beta)/M_{\text{SUSY}}$ are required in order that m_h lie in the $123 - 128$ GeV range.

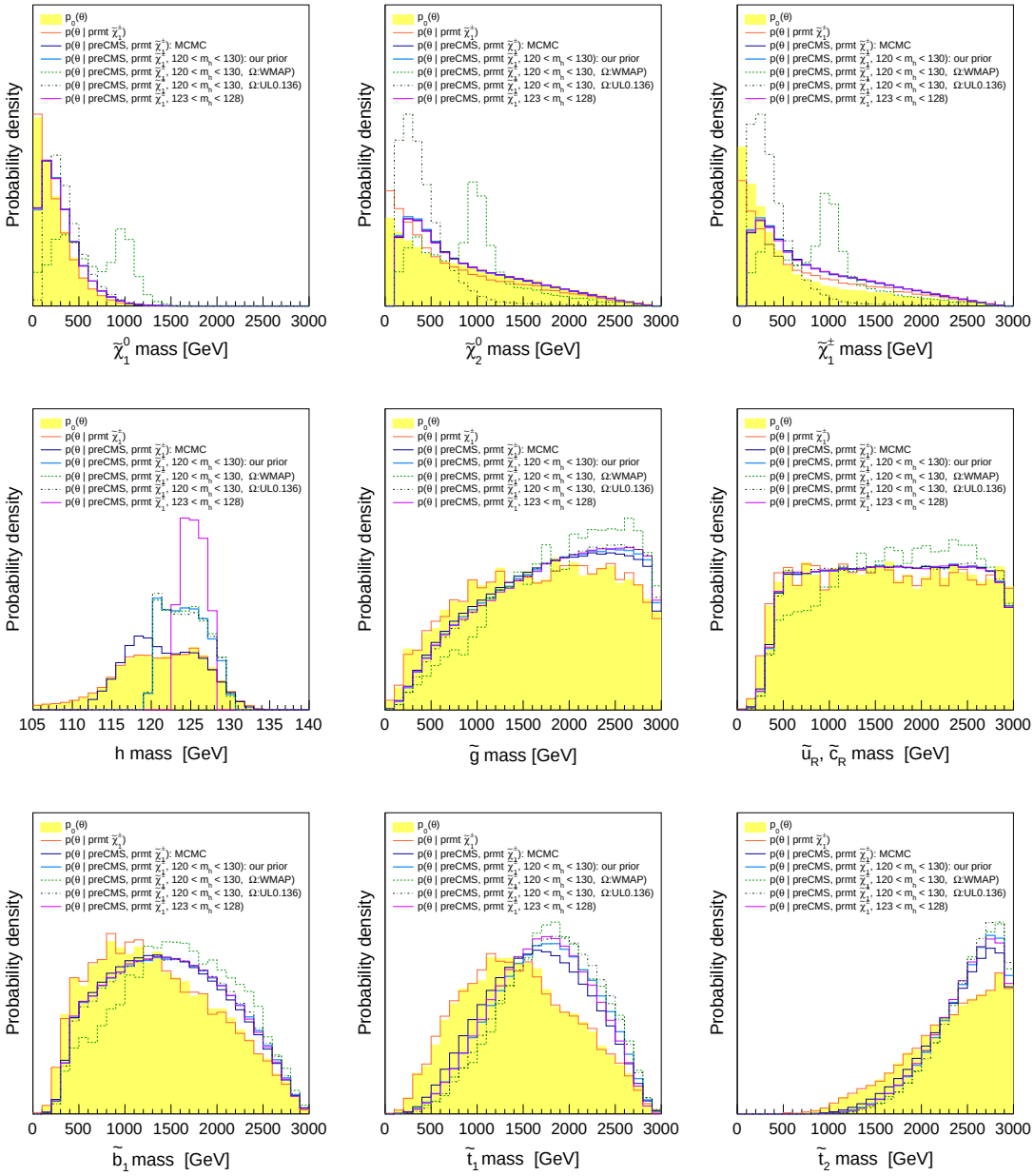

Figure 13: Marginalized 1D posterior densities for selected sparticle masses based on the "preCMS" measurements of Table 1 and various constraints on prompt charginos (prmt), the mass, m_h, of the light neutral Higgs boson, h, and the LSP relic density $\Omega_{\tilde{\chi}_1^0}h^2$ (UL0.136: $\Omega_{\tilde{\chi}_1^0}h^2 < 0.136$, WMAP: $\Omega_{\tilde{\chi}_1^0}h^2 = 0.1123 \pm 0.0035_{\text{obs}} \pm 0.01123_{\text{theory}}$. The yellow histograms show the sampled distributions with a flat prior.

C Results of the CMS analyses

The observed event counts N_l and SM background estimates $B_l \pm \delta B_l$ for each of the implemented analyses, taken from the official results of these analyses, are listed in Tables 3 to 11. Each of these analyses was performed on each pMSSM point as described in Section 3.2 to obtain the signal yields s_i for each search region in each analysis.

Table 3: Signal search regions, observed event counts N_l and SM background estimates $B_l \pm \delta B_l$ for the hadronic $H_T + H_T^{miss}$ search (CMS-SUS-12-011) [42].

Search region		Observed event count	SM BG estimate
H_T(GeV)	H_T^{miss}(GeV)	(N_l)	$(B_l \pm \delta B_l)$
$500-800$	$200-350$	1269	1154 ± 128
$500-800$	$350-500$	236	225 ± 29
$500-800$	$500-600$	22	31.3 ± 5.9
$500-800$	>600	6	8.3 ± 3.2
$800-1000$	$200-350$	177	197 ± 35
$800-1000$	$350-500$	24	29.8 ± 7.5
$800-1000$	$500-600$	6	10.8 ± 4.0
$800-1000$	>600	5	5.0 ± 1.9
$1000-1200$	200-350	71	66 ± 15
$1000-1200$	350-500	12	13.8 ± 5.5
$1000-1200$	>500	4	6.1 ± 2.3
$1200-1400$	200-350	29	25.2 ± 8.9
$1200-1400$	>350	8	5.4 ± 2.3
>1400	>200	16	19.0 ± 9.4

Table 4: Signal search regions, observed event counts N_l and SM background estimates $B_l \pm \delta B_l$ for the hadronic $H_T + E_T^{miss} + b-$jets search (CMS-SUS-12-003) [43].

	Search region			Observed event count	SM BG estimate
	H_T(GeV)	E_T^{miss}(GeV)	$N_{b\text{-jets}}$	(N_l)	$(B_l \pm \delta B_l)$
1BL	>400	>250	≥ 1	478	477 ± 46
1BT	>500	>500	≥ 1	11	6.4 ± 2.8
2BL	>400	>250	≥ 2	146	153 ± 24
2BT	>600	>300	≥ 2	45	26.8 ± 5.6
3BL	>400	>250	≥ 3	22	19.3 ± 7.5

Table 5: Signal search regions, observed event counts N_l and SM background estimates $B_l \pm \delta B_l$ for the hadronic $H_T + E_T^{miss} + \tau$s search (CMS-SUS-12-004) [44].

Search region	Observed event count (N_l)	SM BG estimate ($B_l \pm \delta B_l$)
1 τ	28	29.3 $\pm$ 3.6
$\geq$ 2 τ	9	7.94 $\pm$ 1.17

Table 6: Signal search regions, observed event counts N_l and SM background estimates $B_l \pm \delta B_l$ for the hadronic monojet $+E_T^{miss}$ search (CMS-EXO-11-059) [45].

Search region E_T^{miss}(GeV)	Observed event count (N_l)	SM BG estimate ($B_l \pm \delta B_l$)
$\geq$ 250	7584	7842 $\pm$ 367
$\geq$ 300	2774	2757 $\pm$ 167
$\geq$ 350	1142	1225 $\pm$ 101
$\geq$ 400	522	573 $\pm$ 65

Table 7: Signal search regions, observed event counts N_l and SM background estimates $B_l \pm \delta B_l$ for the same sign di-lepton search (CMS-SUS-11-010) [46].

	Search region $H_T >$ (GeV)	Search region $E_T^{miss} >$ (GeV)	Observed event count (N_l)	SM BG estimate ($B_l \pm \delta B_l$)
high lepton p_T (hgh lpT)				
1	80	120	24	34.1 $\pm$ 12.2
2	200	120	21	22.6 $\pm$ 8.3
3	450	50	11	13.0 $\pm$ 4.9
4	450	120	4	4.9 $\pm$ 2.6
5	450	0	16	23.6 $\pm$ 8.4
low lepton p_T (low lpT)				
2	200	120	28	35.0 $\pm$ 13.4
3	450	50	18	18.8 $\pm$ 7.1
4	450	120	6	6.6 $\pm$ 2.8
τ-channels				
4	80	120	6	7.1 $\pm$ 2.8

Table 8: Signal search regions, observed event counts N_l and SM background estimates $B_l \pm \delta B_l$ for the opposite sign di-lepton search (CMS-SUS-11-011) [47].

Search region	H_T (GeV)	E_T^{miss} (GeV)	Observed event count (N_l)	SM BG estimate ($B_l \pm \delta B_l$)
light lepton channels, overlapping bins				
high E_T^{miss}	> 300	> 275	30	21 ± 12.0
high H_T	> 600	> 200	29	22 ± 10.2
tight	> 600	> 275	11	11 ± 6.9
low H_T	$\in [125, 300]$	275	6	12 ± 7.5
light lepton channels, exclusive bins, Same Flavor (SF)				
SR1	$\in [300, 600]$	> 275	9	5.7 ± 5.8
SR2	> 600	> 275	6	5.3 ± 4.5
SR3	> 600	$\in [200, 275]$	5	5.6 ± 4.0
SR4	$\in [125, 300]$	> 275	3	6 ± 3.75
light lepton channels, exclusive bins, Oposite Flavor (OF)				
SR1	$\in [300, 600]$	> 275	10	5.7 ± 5.8
SR2	> 600	> 275	5	5.3 ± 4.5
SR3	> 600	$\in [200, 275]$	13	5.6 ± 4.0
SR4	$\in [125, 300]$	275	3	6 ± 3.75
τ-lepton channels				
high E_T^{miss}	> 300	> 275	8	8.5 ± 2.3
high H_T	> 600	> 200	5	6.5 ± 1.9
high tight	> 600	> 275	1	4.0 ± 1.5
high low H_T	$\in [125, 300]$	275	0	1.3 ± 0.7

Table 9: Signal search regions, observed event counts N_l and SM background estimates $B_l \pm \delta B_l$ for the 3-lepton channel of the search for electroweak (EWK) production of charginos and neutralinos (CMS-SUS-12-006) [48].

Search region	m_{ll} (GeV)	m_T (GeV)	Observed event count (N_l)	SM BG estimate ($B_l \pm \delta B_l$)
SR I	< 81	< 100	31	23.0 ± 5.1
SR II	< 81	> 100	3	6.0 ± 1.3
SR III	$\in$ [81,101]	> 100	17	16.6 ± 5.7
SR IV	> 101	> 100	2	2.2 ± 0.5
SR V	> 101	< 100	12	11.0 ± 1.9
CR VI	$\in$ [81,101]	< 100	173	164.9 ± 26.4

Table 10: Signal search regions, observed event counts N_l and SM background estimates $B_l \pm \delta B_l$ for the same-sign di-lepton channel of the search for electroweak (EWK) production of charginos and neutralinos (CMS-SUS-12-006) [48].

Search region	Observed event count (N_l)	SM BG estimate ($B_l \pm \delta B_l$)
ee	2	2.1 ± 1.0
$e\mu$	1	3.1 ± 1.2
$\mu\mu$	0	0.7 ± 0.5

Table 11: Signal search regions, observed event counts N_l and SM background estimates $B_l \pm \delta B_l$ for the channel with two leptons and two jets of the search for electroweak (EWK) production of charginos and neutralinos (CMS-SUS-12-006) [48].

Search region E_T^{miss}(GeV)	Observed event count (N_l)	SM BG estimate ($B_l \pm \delta B_l$)
$\in [30, 60]$	2416	2358 ± 737
$\in [60, 80]$	47	43.4 ± 11.4
$\in [80, 100]$	7	12.0 ± 2.4
$\in [100, 150]$	6	8.8 ± 1.8
$\in [150, 200]$	2	1.9 ± 0.5
≥ 200	0	0.7 ± 0.3

D Designing disjoint analyses

We wish to stress the advantage of working with exclusive, that is disjoint, search regions. Consider Fig. 14. It shows the 1D posterior densities for the $\tilde{g}$ and $\tilde{u}_R$ masses for preCMS and after including the results of the $H_T + H_T^{miss}$ search. The green histograms show the distributions for the 14 exclusive search regions while the red line shows the distribution after combining the 14 regions. As expected, the combined result produces a much more pronounced effect than each of the search regions taken separately. It is an obvious point. But, unfortunately, it is one that is routinely ignored.

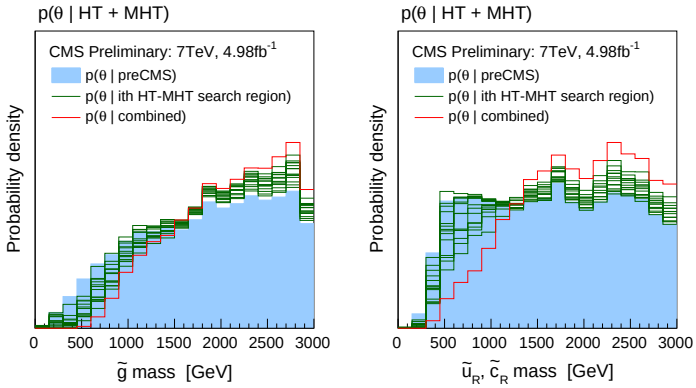

Figure 14: Marginalized 1D posterior probability distributions for $\tilde{g}$ mass and $\tilde{u}_R$ mass. The filled blue histograms in each plot show the posterior densities after preCMS measurements. The line histograms show posterior densities after including the $H_T + H_T^{miss}$ analysis. The green histograms show the distributions for the 14 exclusive $H_T + H_T^{miss}$ search regions given in Table 3, whereas the red line shows the distribution after combining the 14 regions.

E Consequences for the Higgs bosons

As already noticed in Appendix B, once the preCMS constraints are imposed, the impact of the requirement 120 GeV $\leq m_h \leq$ 130 GeV (or 123 GeV $\leq m_h \leq$ 138 GeV) is relatively minor for most particle mass distributions. Indeed the Higgs mass window mainly impacts the distributions of A_t and the related ratio $X_t = (A_t - (\mu/\tan\beta))/\sqrt{m_{\tilde{t}_1} m_{\tilde{t}_2}}$. The former appears in the off-diagonal entries of the stop mass matrix and its size relative to the diagonal entries (roughly the ratio X_t) determines the amount of stop mixing. To achieve $m_h \approx 125$ GeV, large values of $|A_t|$ and $|X_t|$ are needed, with $|X_t|$ only slightly shy of the so-called maximal mixing choice of $|X_t| \sim \sqrt{6}$. This is illustrated in the two bottom-right plots in Fig. 12. The gluino and light stop masses are also shifted to slightly higher values — see Fig. 13. Figure 15 shows the 2D probability distribution in the X_t versus $m_{\tilde{t}_1}$ plane before and after CMS results. In both plots, the bulk of the points have $m_{\tilde{t}_1} > 1$ TeV and $X_t \sim 1.5$ or $X_t \sim -2$. Comparing the right-hand plot, in which the requirement of $|Z_{best}| < 2$ is imposed, to the left-hand plots of the preCMS distribution, we conclude that the CMS analyses currently do not affect the regions preferred by the Higgs mass requirement.

Of greatest immediate interest, however, may be the production/decay rates for the SM-like Higgs boson itself. In particular, how do its signal strengths compare to the measured ones? To answer such questions we define "R" ratios for given initial states X and final states Y:

$$R_X(Y) = \frac{\sigma(X \to h)\mathrm{BR}(h \to Y)}{\sigma_{\mathrm{SM}}(X \to h_{\mathrm{SM}})\mathrm{BR}(h_{\mathrm{SM}} \to Y)}. \tag{19}$$

The initial states of interest are $X = gg$, VBF and Vh. In two doublet models such as the MSSM the scale factor for $X = Vh$ is the same as for $X = VBF$ and so we only plot the latter. The final states of interest are $Y = \gamma\gamma$, ZZ, WW, $\tau\tau$ and bb. In any two doublet model, the scale factor for $Y = WW$ is the same as that for $Y = ZZ$, so again we only plot the latter. Similarly, to first approximation the $\tau\tau$ scale factor is the same as that for bb.

Let us begin with 1D plots. For these plots, we tighten the Higgs mass constraint from 120 GeV $< m_h <$ 130 GeV to 123 GeV $< m_h <$ 128 GeV. This is of course the mass range in which the Higgs-like resonance is observed. In the upper row of Fig. 16, we present probability densities for $R_{gg}(\gamma\gamma)$, $R_{gg}(ZZ)$ and $R_{gg}(bb)$. The corresponding results for the VBF initial state are given in the lower row of Fig. 16. In each case we show the preCMS distribution (blue histograms) and the distribution obtained after imposing $|Z_{best}| < 2$ (red lines). Let us first note that imposing $|Z_{best}| < 2$ in addition to the preCMS requirements has very little impact in these and

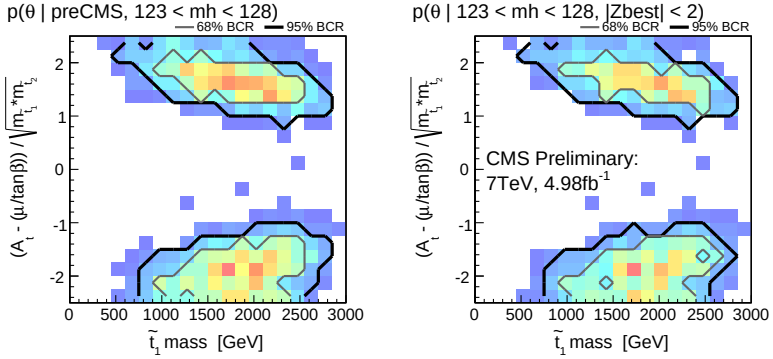

Figure 15: Marginalized 2D posterior densities for X_t vs. $m_{\tilde{t}_1}$. The left plot shows the preCMS posterior density. The right plot includes in addition the requirement $|Z_{best}| < 2$ computed after incorporating the full set of CMS analyses.

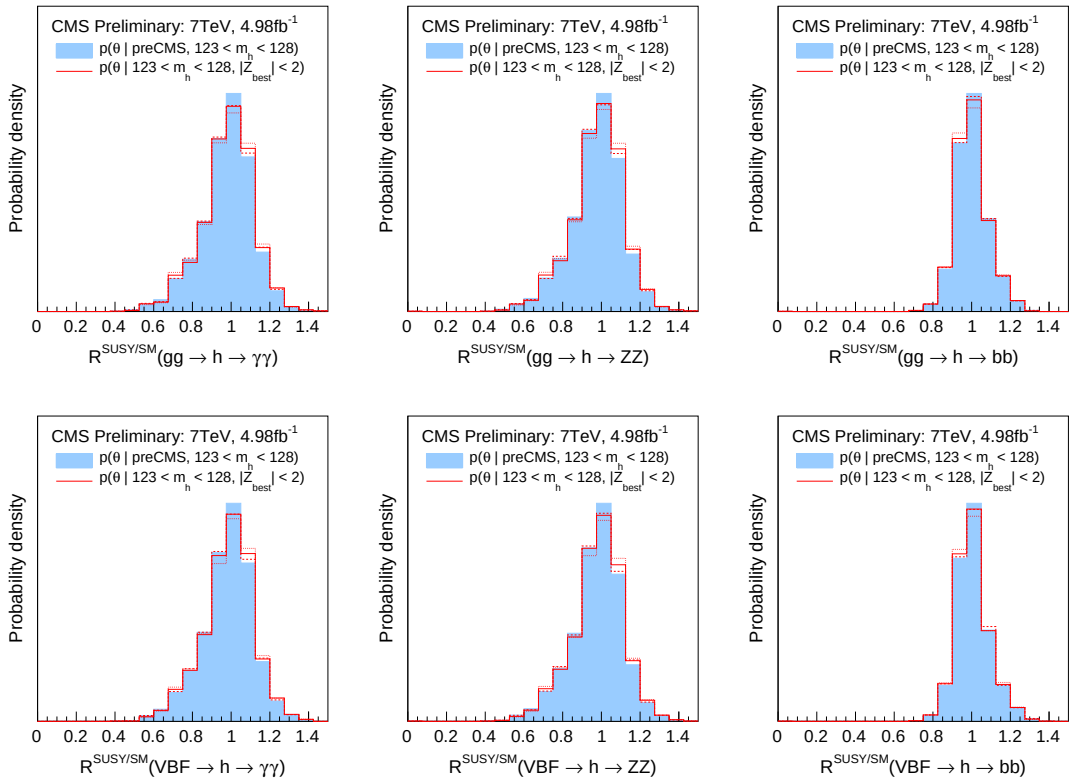

Figure 16: Marginalized 1D posterior probability distributions for $R_{gg}(\gamma\gamma)$, $R_{gg}(ZZ)$ and $R_{gg}(bb)$ (upper row) and for $R_{VBF}(\gamma\gamma)$, $R_{VBF}(ZZ)$ and $R_{VBF}(bb)$ (lower row). The filled blue histograms in each plot show the posterior densities after preCMS measurements. The line histograms show the normalized distributions of points that have best significance $|Z_{best}| < 2$, i.e., points that are not excluded. Solid curves show the distributions obtained from likelihoods (and significances) calculated using the central values of estimated signal counts s, whereas the dashed and dotted lines show the distributions obtained from likelihoods (and significances) calculated using $s - 0.5s$ and $s + 0.5s$ respectively.

all subsequent plots in this section. Thus, all remarks in this section can be taken to apply to both the preCMS and $|Z_{best}| < 2$ distributions. Returning to the R ratios, we observe a strong peaking at values near 1, but ranging with significant probability to values as large as $1.2 - 1.4$ in the $\gamma\gamma$ and ZZ final states, with the bb final state tending to have $R_{gg}(bb)$ values more tightly clustered near unity. Note the slight tendency for the R values in the ZZ final state to be somewhat larger than those in the $\gamma\gamma$ final state. The fact that the R distributions tend to peak at values close to 1 already at the preCMS level implies that the light h is most likely quite SM-like, despite the very large range of MSSM parameter choices being sampled. Therefore, if the measured Higgs signal strengths stay near 1, as is currently the case, it will not be possible to use Higgs observations to single out specific SUSY parameter ranges. Only significant deviations from 1 (with sufficiently small errors) would make it possible to severely constrain SUSY models based on Higgs-sector measurements.

The relationship between the R values in the various final states is obviously also important. In the first row of Fig. 17 we show that the signal strength for the $\gamma\gamma$ final state is strongly correlated with that for the ZZ final state. For instance, $R_{gg,VBF}(\gamma\gamma) \sim 1.2$ is only possible if $R_{gg,VBF}(ZZ) > 1.1$. Note that such enhancement of the rates in these low branching ratio final

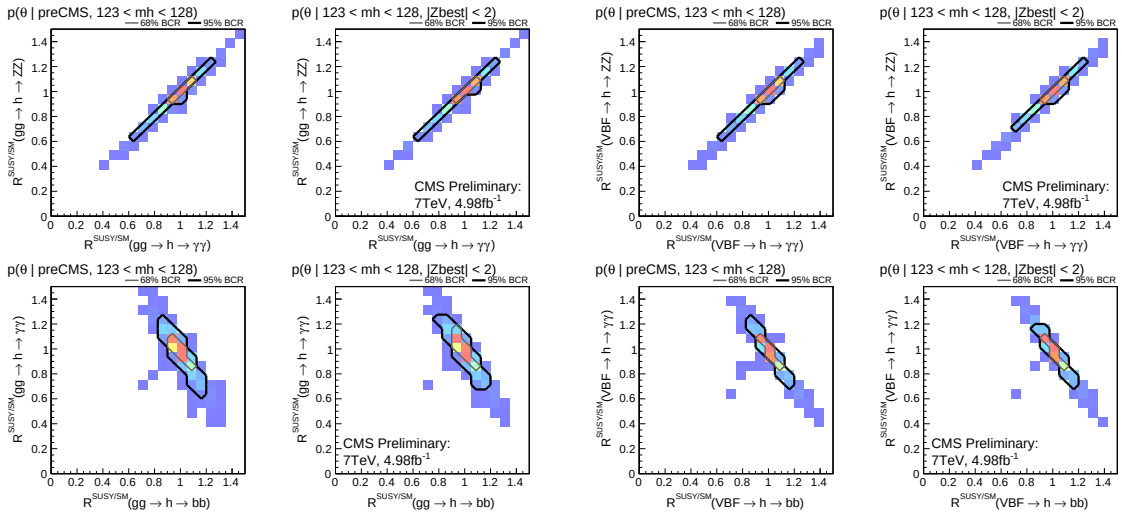

Figure 17: Marginalized 2D posterior probability distributions for $R_{gg}(ZZ)$ vs. $R_{gg}(\gamma\gamma)$, $R_{VBF}(ZZ)$ vs. $R_{VBF}(\gamma\gamma)$, $R_{gg}(\gamma\gamma)$ vs. $R_{gg}(bb)$ and $R_{VBF}(\gamma\gamma)$ vs. $R_{VBF}(bb)$. For each variable pair, the 1st plot shows the preCMS posterior density, and the 2nd plot shows the normalized distributions of points that have best significance $|Z_{best}| < 2$, i.e., points that are not excluded. The grey and black contours enclose the 68% and 95% Bayesian credible regions respectively.

states occurs when the partial width (and hence branching ratio) for the dominant bb final state is suppressed. This is apparent from the second row of Fig. 17. There, we plot the value of $R_{gg}(\gamma\gamma)$ vs. $R_{gg}(bb)$ and $R_{VBF}(\gamma\gamma)$ vs. $R_{VBF}(bb)$. In both cases, we see the inverse correlation noted above; namely, enhanced rates in the $\gamma\gamma$ channel (and also in the ZZ final state) arise when the rates in the bb channel are suppressed, and vice versa. For instance, very roughly, an enhancement of $R_{gg,VBF}(\gamma\gamma) \sim 1.2$ arises only if $R_{gg,VBF}(bb) \lesssim 1$.

Of course, it would be extremely exciting if one of the other Higgs bosons of the MSSM could be detected. To set the general scene, in Fig. 18 we plot the 2D distribution for $m_H - m_A$ vs. m_A. From the figure, we observe that the lowest m_A is of order 500 GeV with $m_A \geq 800$ GeV having greater than 95% probability. Indeed, there is significant probability extending all the way up to 3 TeV and higher. The plot shows that the decoupling result of $m_H \sim m_A$ sets in already for $m_A \sim 500$ GeV. There is a similar very close degeneracy between $m_{H^\pm}$ and m_A, not plotted.

Due to the large masses predicted for the $A, H, H^\pm$, detection of the heavy Higgs bosons will clearly be challenging. Although cross sections for direct production via gg fusion are not dissimilar to the corresponding SM Higgs production cross section for the same mass, their decays are very different. In particular, the A has no tree-level ZZ, WW coupling and will decay primarily to $b\bar{b}$ and $\tau^+\tau^-$ with branching ratios of about 80% and 10%, respectively. In the inclusive final state both these modes have poor mass resolution and large SM backgrounds. Expectations for the H are very similar. This is because for the relevant masses ($m_H > 500$ GeV) one is in the decoupling regime where the H has very small coupling to ZZ, WW and therefore also decays primarily to $b\bar{b}$ and $\tau^+\tau^-$. In particular, even though CMS has strong constraints on the rate for ZZ, WW production in the ≤ 600 GeV region, the associated upper bounds are far above the rates expected from H production.

Probably the most viable search channel for the H and A is $gg \to Ab\bar{b} + Hb\bar{b}$ with $A, H \to \tau\tau$ discovery possibilities are easily assessed given the limits obtained from CMS and the values of $\tan\beta$ that are typical when the Higgs mass is in the $123 - 128$ GeV range. The relevant $\tan\beta$ vs. m_A plot for the 123 GeV $< m_h <$ 128 GeV cut appears in Fig. 19. Comparing to current

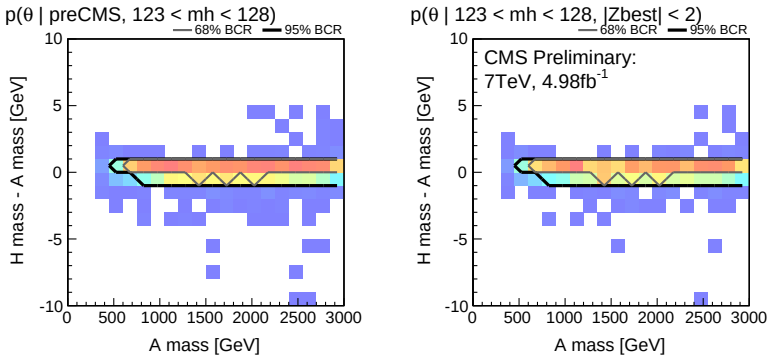

Figure 18: Marginalized 2D posterior probability distributions for $m_H - m_A$ vs. m_A. The 1st plot shows the preCMS posterior density, and the 2nd plot shows the normalized distributions of points that have best significance $|Z_{best}| < 2$, i.e., points that are not excluded. The grey and black contours enclose the 68% and 95% Bayesian credible regions respectively.

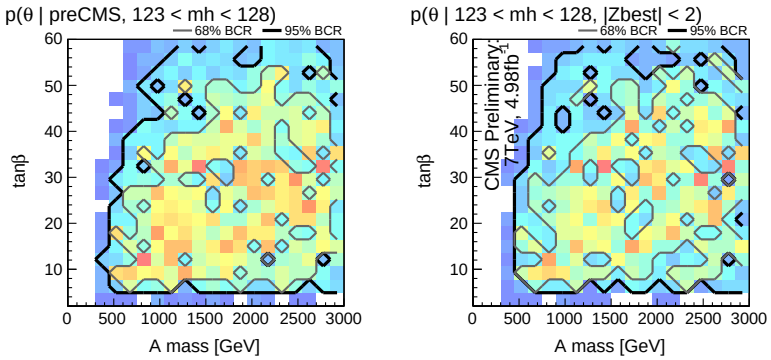

Figure 19: Marginalized 2D posterior probability distributions for $\tan\beta$ vs. m_A with 123 GeV $< m_h <$ 128 GeV required. The 1st plot shows the preCMS posterior density, and the 2nd plot shows the normalized distributions of points that have best significance $|Z_{best}| < 2$, i.e., points that are not excluded. The grey and black contours enclose the 68% and 95% Bayesian credible regions respectively.

limits [49] obtained assuming $m_H \sim m_A$ and neglecting interference (both approximations being adequate given the poor mass resolution in the $\tau\tau$ final state), we find that most points in this plane are allowed. Only a few points at the very highest $\tan\beta$ values at a given m_A would be excluded. Future improvement in the limits can be expected once additional data are analyzed.

Other channels that might allow sensitivity to the heavy Higgs bosons include the production+decay channels $gg \to A \to \gamma\gamma$ and $gg \to H \to \gamma\gamma$. Unfortunately, extremely small cross section times branching ratio values, typically of order $10^{-3} - 10^{-7}$ fb, are predicted. Such cross sections times branching ratio values could only begin to be probed at a high-luminosity LHC. Of course, the irreducible and reducible backgrounds to the $\gamma\gamma$ final state in the high mass region have not been studied and so the viability of seeing a handful of events above the expected background cannot at this time be assessed.

One could consider the channels $gg \to H \to hh$ and $gg \to A \to Zh$. However, it turns out that the branching ratios for $H \to hh$ and $A \to Zh$ are very small throughout the part of parameter space allowed by the preCMS analysis and observation of these final states appears

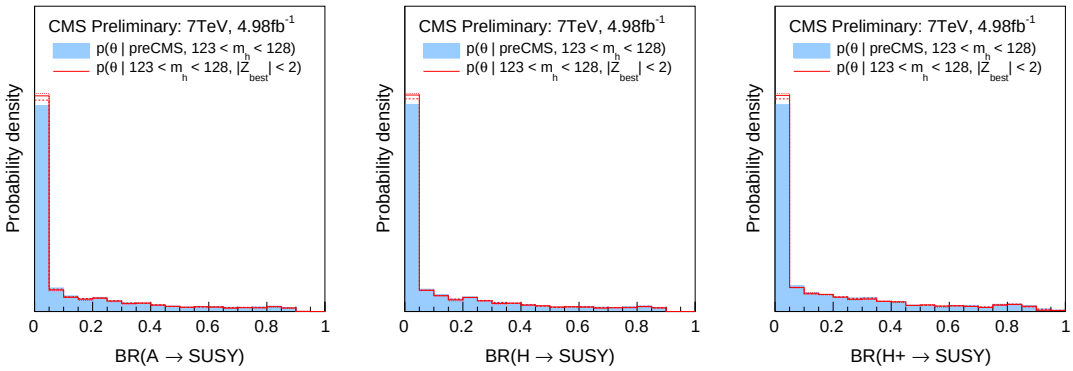

Figure 20: Marginalized 1D posterior probability distributions for BR($A \to$ SUSY), BR($H \to$ SUSY) and BR($H^+ \to$ SUSY), where SUSY represents the sum over all sparticle pair states. The filled blue histograms in each plot show the posterior densities after preCMS measurements. The line histograms show the normalized distributions of points that have best significance $|Z_{best}| < 2$, i.e., points that are not excluded. Solid curves show the distributions obtained from likelihoods (and significances) calculated using the central values of estimated signal counts s, whereas the dashed and dotted lines show the distributions obtained from likelihoods (and significances) calculated using $s - 0.5s$ and $s + 0.5s$ respectively.

very unlikely at the LHC.

Finally, it is interesting to assess the extent to which the $H, A, H^{\pm}$ might be observable via decays into supersymmetric final states. The branching ratios for SUSY decays of these Higgs bosons are displayed in Fig. 20. From these plots, it is clear that for a small, but significant fraction of the preCMS parameter space these Higgs bosons decay with a significant branching ratio to superpartner-pair final states. It is beyond the scope of this paper to pursue the viability of detection in such modes. Note, however, that these superpartner-pair final states are typically not pairs of LSPs but sparticles that give potentially visible signatures. Regarding the h, BR($h \to$ SUSY) (not plotted), where in this case SUSY=$\widetilde{\chi}_1^0\widetilde{\chi}_1^0$, is always very small even when kinematically allowed.

F Consequences for dark matter observables

Although we assume R-parity conservation and a neutralino LSP, we chose not to apply any dark matter (DM) constraints on the neutralino in the sampling of the pMSSM parameter space. We did this to avoid making assumptions about the history of the Universe (such as pure thermal production of particles, only one DM candidate, constant entropy after freeze-out, etc.) as usually enter the "vanilla" DM constraints. Instead, in this section we test the influence of the CMS SUSY searches on DM-related quantities, such as the would-be neutralino relic density, $\Omega_{\tilde{\chi}_1^0}h^2$ (assuming standard cosmology) and the expected spin-dependent (SD) and spin-independent (SI) cross sections for scattering off protons, $\xi\sigma^{\mathrm{SD}}(\tilde{\chi}_1^0 p)$ and $\xi\sigma^{\mathrm{SI}}(\tilde{\chi}_1^0 p)$, respectively, which are relevant for direct dark matter searches.

Figure 21 shows the marginalized 1D posterior density for the neutralino relic density $\Omega_{\tilde{\chi}_1^0}h^2$, comparing the distributions after requiring $|Z_{\mathrm{best}}| < 2$ (lines) to the preCMS distribution (filled blue histogram). For the preCMS distribution, we note that the probability to have a relic density that is too high (too low) is 53.0% (46.2%), while for the 2σ WMAP window $p(0.089 \leq \Omega_{\tilde{\chi}_1^0}h^2 \leq 0.136) \sim 0.8\%$. The $|Z_{\mathrm{best}}| < 2$ distribution has increased weight at very small $\Omega_{\tilde{\chi}_1^0}h^2$.

The 2D posterior probability densities of $\Omega_{\tilde{\chi}_1^0}h^2$, $\xi\sigma^{\mathrm{SI}}(\tilde{\chi}_1^0 p)$ and $\xi\sigma^{\mathrm{SD}}(\tilde{\chi}_1^0 p)$ versus the LSP mass are shown in Fig. 22. A rescaling factor $\xi = \Omega_{\tilde{\chi}_1^0}h^2/0.1123$ is applied for the $\tilde{\chi}_1^0 p$ scattering cross section to allow comparison with the limits from direct DM detection experiments. The effect of requiring $|Z_{\mathrm{best}}| < 2$ is compared to the preCMS posterior densities. In the preCMS posterior density, the 95% Bayesian credible region (BCR) for a relic density of about 0.1 has a lower boundary that lies (roughly) around $m_{\tilde{\chi}_1^0} \sim 200$ GeV and an upper boundary that is located at $m_{\tilde{\chi}_1^0} \sim 0.5 - 1$ TeV. For $|Z_{\mathrm{best}}| < 2$, these upper and lower boundaries are shifted to somewhat higher $m_{\tilde{\chi}_1^0}$ values. The possible complementarity between collider and astrophysics experiments for pinning down the nature of DM (and eventually testing the standard cosmological model) hence becomes apparent, though the influence of current LHC results is still marginal.

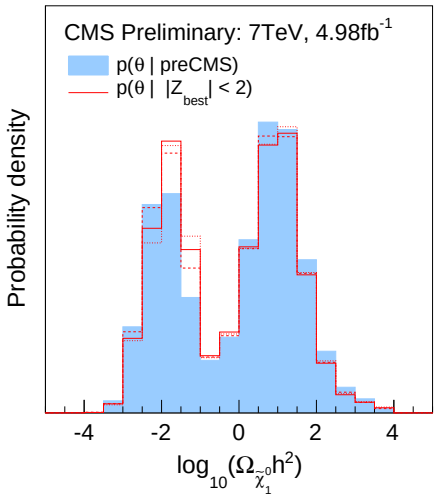

Figure 21: Marginalized 1D posterior probability distributions for the neutralino relic density $\Omega_{\tilde{\chi}_1^0}h^2$. The filled blue histogram in the plot shows the posterior density after preCMS measurements. The line histograms show the posterior densities for the non-excluded $|Z_{\text{best}}| < 2$ points. The solid curve shows the posterior density obtained from likelihoods calculated using the central values of estimated signal counts s, whereas the dashed and dotted lines show the posterior density obtained from likelihoods calculated using $s - 0.5s$ and $s + 0.5s$ respectively.

G Exploring the unexplored

In order to quantify what regions of the pMSSM have been missed by the searches considered in this study, a set of pMSSM points has been defined for which $|Z| \leq 2$. This set of points are referred to as the "unexplored" or non-excluded points. Note that, evidently, the points are "unexplored" only with respect to the analyses we have included in this study (see Sec. 3.3). A total of 4504 of all 7205 points are found in this set. In the following, the characteristics of these points will be discussed, focusing on those "unexplored" points that have a large production cross section (i.e., with $\sigma > 10$ fb). Of the 4504 points, 2198 fulfill this criterion. We refer to the latter as "unexplored high-σ points". Fig. 23 shows the total production cross sections of the unexplored pMSSM points.

G.1 Unexplored high-σ points

Why do the 2198 unexplored pMSSM points with $\sigma^{\text{prod}} > 10$ fb escape detection? This question shall be answered in two steps: first, we shall explore the production mechanism of the unexplored points. Second, and more importantly, the pMSSM points will be decomposed into Simplified Model Spectra (SMS) [7] (see also [50, 51]). The problematic pMSSM points can then easily be categorized and scrutinized. Fig. 24 shows the production modes of the 2198 unexplored high-σ points. It can be seen that EWK production of charginos and neutralinos ("nn"), weakino for short, and squark-pair ("ss") production dominates, with some contributions from gluino-pair production ("gg"), neutralino-squark ("ns"), and squark-gluino associate production ("sg"). Table 12 lists the overall fractions for the various production mechanisms.

These cases shall now be discussed individually.

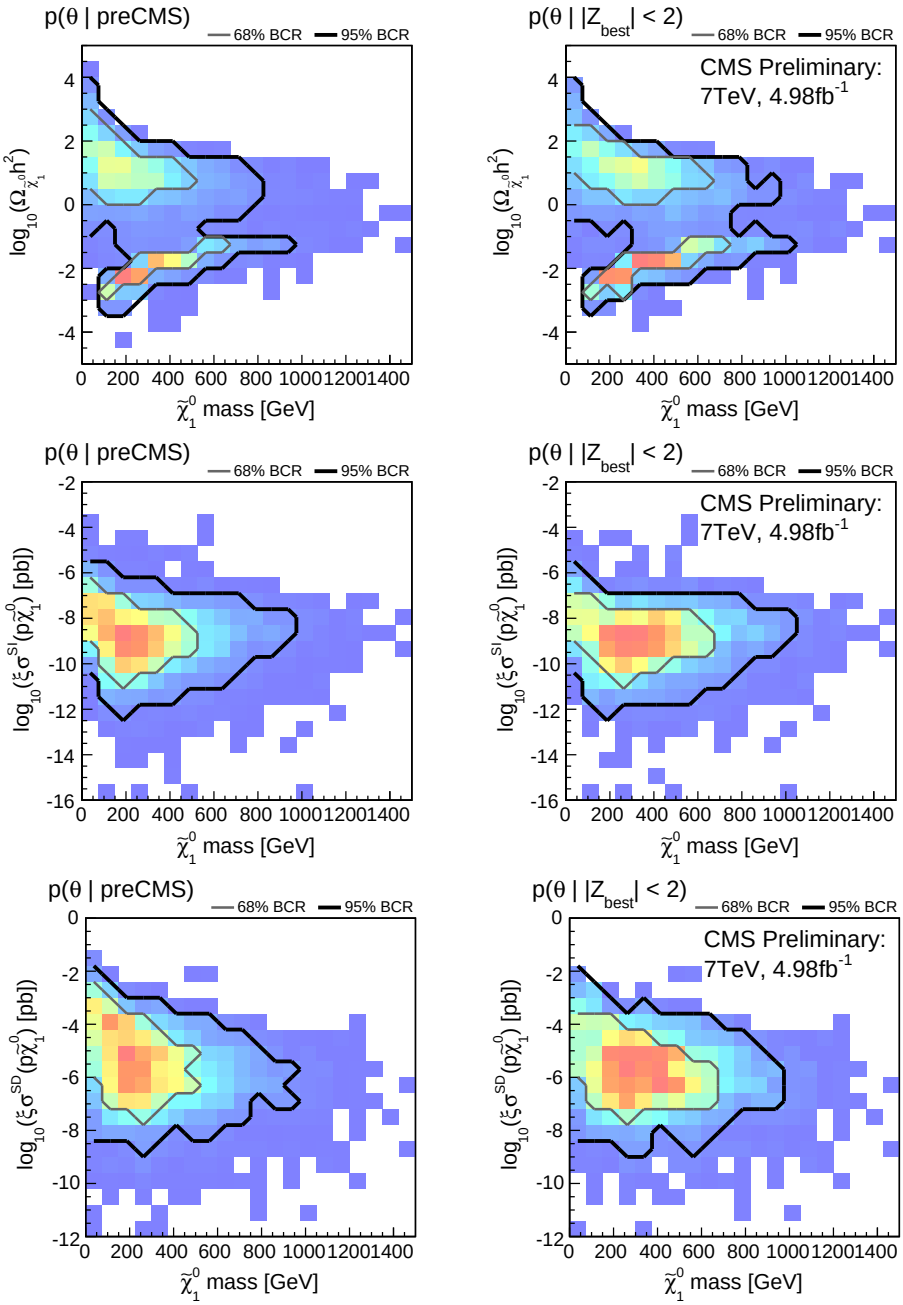

Figure 22: Marginalized 2D posterior probability distributions for neutralino relic density $\Omega_{\tilde{\chi}_1^0}h^2$ (top row), spin-independent direct DM detection cross section $\xi\sigma^{\mathrm{SI}}$ (middle row), and spin-dependent direct DM detection cross section $\xi\sigma^{\mathrm{SD}}$ (bottom row) versus LSP mass. The rescaling factor $\xi = \Omega_{\tilde{\chi}_1^0}h^2/0.1123$. For each variable pair, the 1st plot shows the preCMS posterior density, and the 2nd plot shows the normalized distributions of points that have best significance $|Z_{\mathrm{best}}| < 2$, i.e., points that are not excluded. The grey and black contours enclose the 68% and 95% Bayesian credible regions respectively.

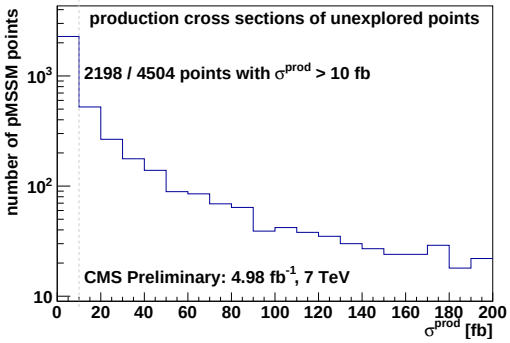

Figure 23: Number of unexplored pMSSM points, as a function of the production cross section.

Table 12: Overall fractions of production mechanisms in the unexplored high-σ points. Eg. in 40.4% of all unexplored high-σ pMSSM points, weakino ("nn") production amounts to more than 90% of all events.

	Fraction of pMSSM points [%] for which channel contributes ...			
channnel	$> 90\%$	50 - 90%	10 - 50%	$< 10\%$
nn	40.4	14	11.8	33.8
ss	11.9	18.1	12.8	57.2
gg	1.5	2.1	2.6	93.9
sg	0.0	0.6	6.1	93.3
ns	0.0	0.3	6.3	93.4
tt	0.3	0.5	1.8	97.4
ll	0.1	0.1	1.6	98.2
ng	0.0	0.0	0.3	99.7

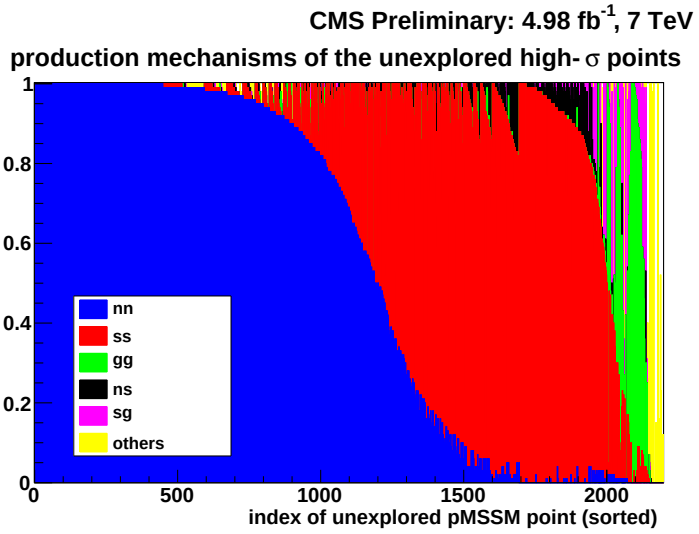

Figure 24: Production mechanisms for unexplored high-σ pMSSM points, "point-for-point" – the x-axis simply sorts the 2198 points. Weakino and squark-squark productions dominate.

G.2 Decomposition into Simplified Model Spectra

The discussion about the decomposition into Simplified Model adheres to the naming conventions introduced previously in Refs [50], [7]. For cases that are not discussed in Ref. [50], the naming convention will be extended in the following manner. All names start with a "T", which stands for "topology". In the case of gluino-gluino production the "T" is followed by an odd number, depending on the assumption about the gluino decay. Direct decays to quarks and the LSP are labelled "1"; in the case of an intermediate state appearing on one leg of the simplified model but not on the other, a "3" is appended, while "5" denotes intermediate states on both legs. For squark-squark production, even numbers are used: "2" denotes direct decay to the LSP, while "4" and "6" code for topologies with intermediate mass states on one and two legs, respectively. Postfixes specify details about the final states. For example, T1tttt represents gluino production, where both gluinos decay via $\tilde{g} \to tt\widetilde{\chi}_1^0$; T2bb is sbottom-sbottom production, with sbottoms decaying via $\tilde{b} \to b\widetilde{\chi}_1^0$. The symbol TChi denotes weakino production. The occurence of on-shell gauge or Higgs bosons is denoted by the "final state"; for example, TChiwz denotes the production of a chargino and a heavy neutralino, where $\widetilde{\chi}_1^\pm \to W^\pm\widetilde{\chi}_1^0$ and $\widetilde{\chi}_2^0 \to Z\widetilde{\chi}_1^0$. In the case of a three-body decay, the weakinos are named directly: TChiC1N2 indicates the production of a chargino (C1) and a heavy neutralino (N2). The LSP is marked as "N1". TNS represents squark-weakino production. See Ref. 25 for examples.

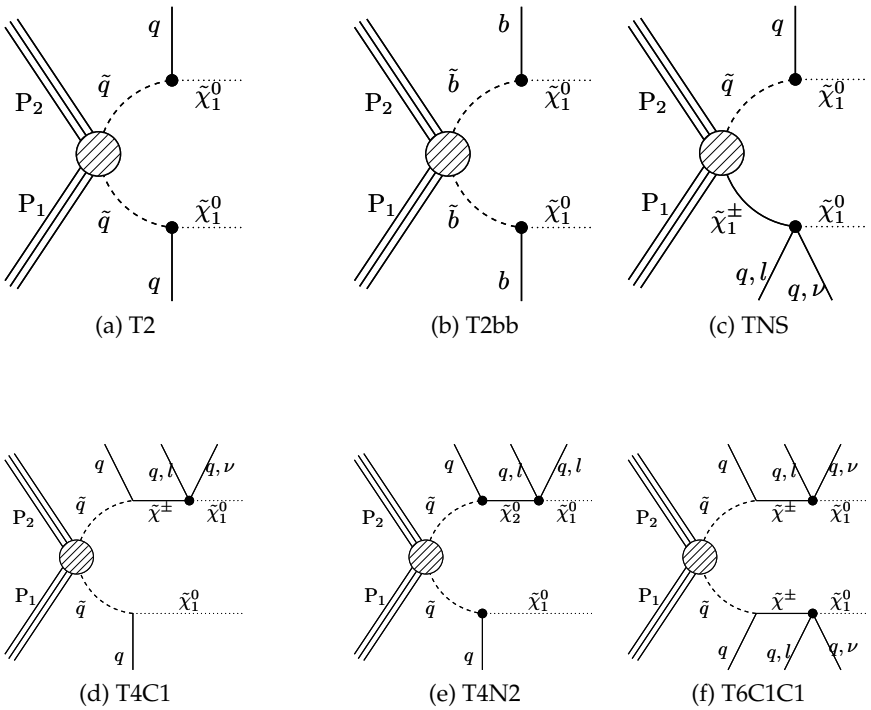

(a) T2 (b) T2bb (c) TNS

(d) T4C1 (e) T4N2 (f) T6C1C1

Figure 25: A few simplified models for squark production.

G.3 The case of weakino production

Of the 2198 high-σ points, 1188 are predominantly weakino production – the fraction of weakino production is larger than 50%. Fig. 27(left) shows the lengths of the SUSY decay chains: the number of SUSY particles from the production particle to the LSP is counted for each leg individually. For example, the decay $\widetilde{\chi}_2^0 \to Z\widetilde{\chi}_1^0$ has a length of two. The percentages in this plot take into account the point's $\sigma \times BR$, i.e. they are weighted with the cross sections. Only the

weakino points have been considered. It can be seen that almost one half (45%) of all cases correspond to the production of two heavy weakinos that decay directly to the LSP, while the other half (46%) of all events have a heavy weakino on one side, and the LSP on the other. The SMS categorization in the electroweak sector differentiates between the different neutralino states (N1,N2,N3) and the charginos (C1,C2,C3). The symbols for on-shell W, Z, and Higgs bosons are postfixed. The special case of TChiN2C1wz is denoted by TChiwz. Equivalently, TChizz and TChiww are "nicknames" for TChiN2N2zz and TChiC1C1ww. Figs. 26 shows the most dominant models.

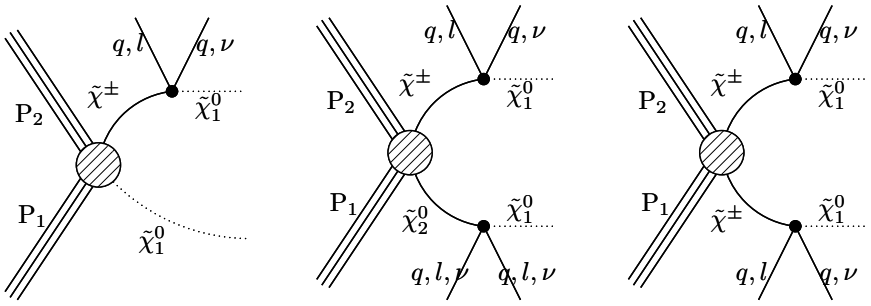

Figure 26: The most important simplified models for the electroweak case.

Fig. 27(right) shows the leading SMS topologies for these 1188 weakino production points, the pMSSM points have been weighted with the production cross sections. Production of a chargino with the LSP (TChiC1N1) is the dominant case. Fig. 28(left) shows the mass splitting between the heavier weakinos and the LSP, with

$$\Delta(\text{EWK}) = \min(m_{\tilde{\chi}_2^0}, m_{\tilde{\chi}_1^\pm}) - m_{\tilde{\chi}_1^0} \tag{20}$$

The unexplored points tend to have very small mass splittings. Typically, mass splittings < 1 GeV are favored: 803 of the 1188 unexplored high-σ weakino points have a mass splitting of $\Delta(\text{EWK}) < 5$ GeV!

G.4 The case of squark-pair production

Of the 2198 high-σ points, 757 are predominantly squark-squark production. (We required that more than 50% of the total production cross section pertain to squark-squark or squark-antisquark production.) Fig. 29 shows the leading SMS topologies of the unexplored points, again taking the pMSSM points' cross sections into account. See Fig. 25 for the Feynman graphs of the topologies. Direct decays are dominant. Fig. 30 shows the distribution of the minimal

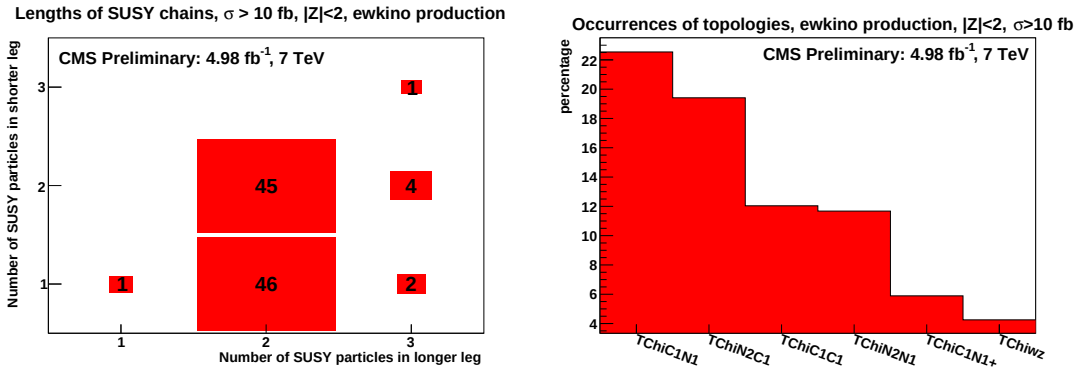

Figure 27: Lengths of the SUSY decay chains, counting from the SUSY mother particle to the LSP, for both legs, given as a percentage, for the high-σ electroweak sample (left), and leading SMS topologies for the case of weakino production (right). Chargino – LSP (TChiC1N1) production dominates, followed by the production of a chargino and a heavy neutralino (TChiN2C1) and the production of two charginos (TChiC1C1). The plus sign in TChiC1N1+ indicates the production of a chargino and the LSP with a non-trivial decay of the chargino. All numbers have been weighted with the production cross sections times branching ratios.

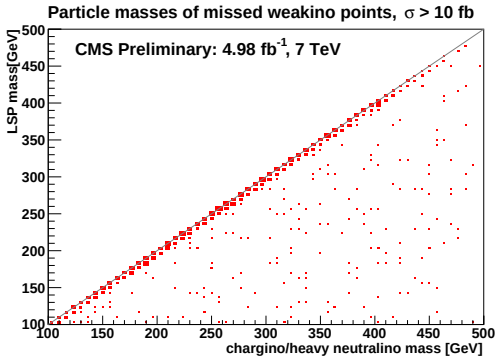

Figure 28: Chargino / heavy neutralino mass versus LSP mass.

mass splitting $\Delta(q) = m_{\tilde{q}} - m_{chiz}$. A large fraction of our unexplored points have a mass splitting < 100 GeV. Note that we defined an unexplored point to be a pMSSM point that has been missed by the analyses given in Sec. 3.3. To study if these points can be reached with dedicated hadronic low-HT searches is an interesting challenge for the future.

G.5 Consistency between pMSSM results and SMS results

A simple but efficient cross check has been performed between the pMSSM significances (Z, Eq. 9) and the published simplified models 95% upper limits on the production cross section, for the SUS-12-011 analysis [42]. For every pMSSM point the "leading" simplified models result is used, if and only if it is known to describe > 50 % of the events at this point. Fig. 31 shows the points that have *not* been excluded by the SMS results in black; the points that *can* be excluded by the SMS results are shown in red. An SMS result is said to exclude a point if the pMSSM cross section times branching ratio for this particular simplified model exceeds the 95% CL upper limit. This criterion of 95% CL corresponds to a $|Z|$ value of 1.96; thus, the majority (though not all) of the "missed points" should have Z values lower than ≈ 2, while practically all "excluded" points must have $Z < -2$, or $|Z| > 2$ in our case, since there are no points with $Z > 2$. This is indeed the case.

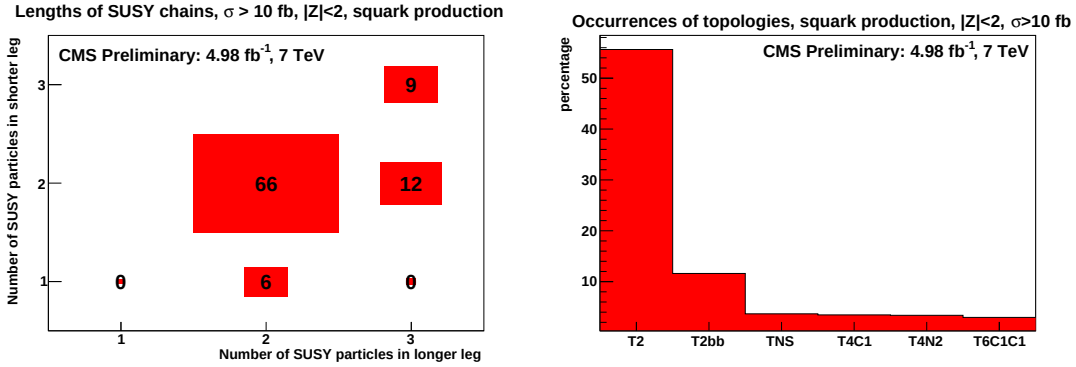

Figure 29: Lengths of the SUSY decay chains (left) and occurrences of SMS topologies for the squark production cases (right). Direct decays $\tilde{q} \to q\tilde{\chi}^0$ and $\tilde{b} \to b\tilde{\chi}^0$ dominate. All numbers have been weighted with the production cross sections times branching ratios.

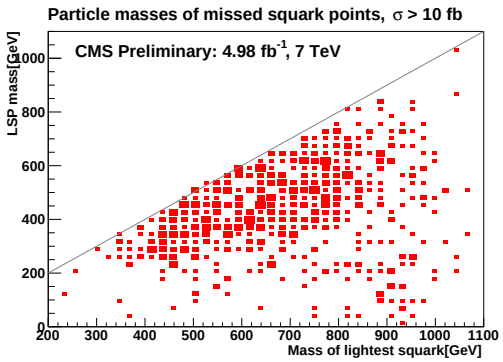

Figure 30: Mass of lightest squark versus LSP mass.

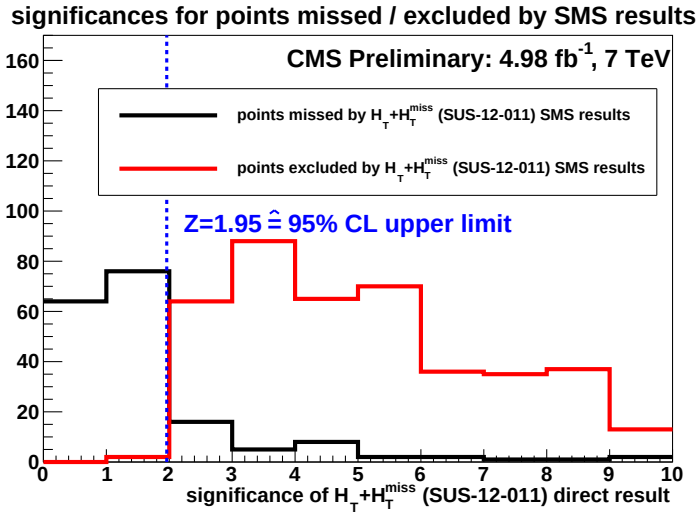

Figure 31: Cross check between pMSSM results and SMS results, for SUS-12-011. The histograms show the distributions of $|Z|$ values, which are calculated through implementing the full analysis chain on each point. Points with $Z > 2$ are excluded whereas points with $|Z| < 2$ are unexplored (note that points with $Z > 2$ would point to discovery, however we do not have any such points in our list, therefore our set of points with $|Z| > 2$ fully consist of excluded points with $Z < -2$). The red histogram shows the $|Z|$ distribution for points that are excluded by the SMSs, and the black curve shows the Z distribution for the points that are missed, or unexplored by the SMSs. The red histogram almost always has $|Z| > 2$, which means that the points excluded by the SMSs are also excluded by the full analysis. The black histogram almost always has $|Z| < 2$, which means that the points unexplored by the SMSs are also unexplored by the full analysis. A small part of the black histogram lies beyond $|Z| > 2$, corresponding to points missed by the SMS results but excluded by the direct analysis.

References

[1] G. Aad *et al.* [ATLAS Collaboration], "Observation of a new particle in the search for the Standard Model Higgs boson with the ATLAS detector at the LHC," Phys. Lett. B **716**, 1 (2012) [arXiv:1207.7214 [hep-ex]].

[2] S. Chatrchyan *et al.* [CMS Collaboration], "Observation of a new boson at a mass of 125 GeV with the CMS experiment at the LHC," Phys. Lett. B **716**, 30 (2012) [arXiv:1207.7235 [hep-ex]].

[3] S. P. Martin, "A Supersymmetry primer," In *Kane, G.L. (ed.): Perspectives on supersymmetry II* 1-153 [hep-ph/9709356].

[4] D. J. H. Chung, L. L. Everett, G. L. Kane, S. F. King, J. D. Lykken and L. -T. Wang, "The Soft supersymmetry breaking Lagrangian: Theory and applications," Phys. Rept. **407**, 1 (2005) [hep-ph/0312378].

[5] A. H. Chamseddine, R. L. Arnowitt, P. Nath, Phys. Rev. Lett. **49**, 970 (1982); R. Barbieri, S. Ferrara, C. A. Savoy, Phys. Lett. **B119**, 343 (1982); L. E. Ibanez, Phys. Lett. **B118**, 73 (1982); L. J. Hall, J. D. Lykken, S. Weinberg, Phys. Rev. **D27**, 2359-2378 (1983); for a review see, e.g., P. Nath, hep-ph/0307123.

[6] G. L. Kane, C. F. Kolda, L. Roszkowski, J. D. Wells, Phys. Rev. **D49**, 6173 (1994), hep-ph/9312272; H. Baer, C. -H. Chen, R. B. Munroe, F. E. Paige, X. Tata, Phys. Rev. **D51**, 1046-1050 (1995), hep-ph/9408265.

[7] S. Chatrchyan *et al.* [CMS Collaboration], "Interpretation of searches for supersymmetry with simplified models," arXiv:1301.2175 [hep-ex].

[8] A. Djouadi *et al.* [MSSM Working Group Collaboration], "The Minimal supersymmetric standard model: Group summary report," hep-ph/9901246.

[9] S. Sekmen, S. Kraml, J. Lykken, F. Moortgat, S. Padhi, L. Pape, M. Pierini, H. B. Prosper and M. Spiropulu, "Interpreting LHC SUSY searches in the phenomenological MSSM," JHEP **1202**, 075 (2012) [arXiv:1109.5119 [hep-ph]].

[10] S. Chatrchyan *et al.* [CMS Collaboration], "Search for Supersymmetry at the LHC in Events with Jets and Missing Transverse Energy," Phys. Rev. Lett. **107**, 221804 (2011) [arXiv:1109.2352 [hep-ex]].

[11] CMS Collaboration, "Search for new physics with same-sign isolated dilepton events with jets and missing energy," CMS-PAS-SUS-11-010.

[12] CMS Collaboration, "Search for new physics in events with opposite-sign dileptons and missing transverse energy," CMS-PAS-SUS-11-011.

[13] C. P. Robert, "The Bayesian Choice: from Decision-Theoretic Foundations to Computational Implementation," 2nd ed. (Springer, New York, 2007).

[14] A. O'Hagan, "Bayesian Inference," Kendall's Advanced Theory of Statistics Vol. 2B (Edward Arnold, London, 1994).

[15] C. F. Berger, J. S. Gainer, J. L. Hewett and T. G. Rizzo, "Supersymmetry Without Prejudice," JHEP **0902**, 023 (2009) [arXiv:0812.0980 [hep-ph]].

[16] J. A. Conley, J. S. Gainer, J. L. Hewett, M. P. Le and T. G. Rizzo, "Supersymmetry Without Prejudice at the LHC," Eur. Phys. J. C **71**, 1697 (2011) [arXiv:1009.2539 [hep-ph]].

[17] J. A. Conley, J. S. Gainer, J. L. Hewett, M. P. Le and T. G. Rizzo, "Supersymmetry Without Prejudice at the 7 TeV LHC," [arXiv:1103.1697 [hep-ph]].

[18] S. S. AbdusSalam, B. C. Allanach, F. Quevedo, F. Feroz and M. Hobson, "Fitting the Phenomenological MSSM," Phys. Rev. D **81**, 095012 (2010) [arXiv:0904.2548 [hep-ph]].

[19] M. Farina, M. Kadastik, D. Pappadopulo, J. Pata, M. Raidal and A. Strumia, "Implications of XENON100 and LHC results for Dark Matter models," Nucl. Phys. B **853**, 607 (2011) [arXiv:1104.3572 [hep-ph]].

[20] A. Arbey, M. Battaglia and F. Mahmoudi, "Implications of LHC Searches on SUSY Particle Spectra: The pMSSM Parameter Space with Neutralino Dark Matter," Eur. Phys. J. C **72** (2012) 1847 [arXiv:1110.3726 [hep-ph]].

[21] B. C. Allanach, "SOFTSUSY: a program for calculating supersymmetric spectra," Comput. Phys. Commun. **143**, 305 (2002) [hep-ph/0104145].

[22] F. Mahmoudi, "SuperIso v2.3: A Program for calculating flavor physics observables in Supersymmetry," Comput. Phys. Commun. **180**, 1579 (2009) [arXiv:0808.3144 [hep-ph]].

[23] G. Belanger, F. Boudjema, A. Pukhov and A. Semenov, "MicrOMEGAs: A Program for calculating the relic density in the MSSM," Comput. Phys. Commun. **149**, 103 (2002) [hep-ph/0112278].

[24] G. Belanger, F. Boudjema, A. Pukhov and A. Semenov, "micrOMEGAs: Version 1.3," Comput. Phys. Commun. **174**, 577 (2006) [hep-ph/0405253].

[25] G. Belanger, F. Boudjema, A. Pukhov and A. Semenov, "Dark matter direct detection rate in a generic model with micrOMEGAs 2.2," Comput. Phys. Commun. **180**, 747 (2009) [arXiv:0803.2360 [hep-ph]].

[26] A. Djouadi, M. M. Muhlleitner and M. Spira, "Decays of supersymmetric particles: The Program SUSY-HIT (SUspect-SdecaY-Hdecay-InTerface)," Acta Phys. Polon. B **38**, 635 (2007) [hep-ph/0609292].

[27] P. Z. Skands, B. C. Allanach, H. Baer, C. Balazs, G. Belanger, F. Boudjema, A. Djouadi and R. Godbole *et al.*, "SUSY Les Houches accord: Interfacing SUSY spectrum calculators, decay packages, and event generators," JHEP **0407**, 036 (2004) [hep-ph/0311123].

[28] Y. Amhis *et al.* [Heavy Flavor Averaging Group Collaboration], "Averages of B-Hadron, C-Hadron, and tau-lepton properties as of early 2012," arXiv:1207.1158 [hep-ex].

[29] M. Misiak, H. M. Asatrian, K. Bieri, M. Czakon, A. Czarnecki, T. Ewerth, A. Ferroglia and P. Gambino *et al.*, "Estimate of B(anti-B —¿ X(s) gamma) at O(alpha(s)**2)," Phys. Rev. Lett. **98**, 022002 (2007) [hep-ph/0609232].

[30] ALTAS, CMS and LHCb Collaborations, "Search for the rare decays Bs and B0 to dimuons at the LHC with the ATLAS, CMS and LHCb experiments," CMS-PAS-BPH-12-009

[31] R. Aaij *et al.* [LHCb Collaboration], "First evidence for the decay Bs -¿ mu+ mu-," Phys. Rev. Lett. **110** (2013) 021801 [arXiv:1211.2674].

[32] K. Nakamura *et al.* [Particle Data Group Collaboration], "Review of particle physics," J. Phys. G **37**, 075021 (2010).

[33] K. Hagiwara, R. Liao, A. D. Martin, D. Nomura and T. Teubner, "$(g-2)_m u$ and $alpha(M_Z^2)$ re-evaluated using new precise data," J. Phys. G **38** (2011) 085003 [arXiv:1105.3149 [hep-ph]].

[34] ATLAS and CMS Collaborations, "Combination of ATLAS and CMS results on the mass of the top quark using up to 4.9 fb^{-1} of data," ATLAS-CONF-2012-095, CMS-PAS-TOP-12-001

[35] Joint LEP2 SUSY Working Group, the Aleph, Delphi, L3 and Opal collaborations, `http://lepsusy.web.cern.ch/lepsusy/`

[36] A. A. Markov, *Extension of the limit theorems of probability theory to a sum of variables connected in a chain*, reprinted in Appendix B of: R. Howard, *Dynamic Probabilistic Systems, volume 1: Markov Chains*, John Wiley and Sons, 1971;
N. Metropolis, A.W. Rosenbluth, M.N. Rosenbluth, A.H. Teller, and E. Teller, Journal of Chemical Physics, 21(6):1087-1092, 1953; W.K. Hastings, Biometrika, 57(1):97–109, 1970;
B.A. Berg, *Markov Chain Monte Carlo Simulations And Their Statistical Analysis*, (World Scientific, 2004).

A. O'Hagan, *Bayesian Inference*, Kendall's Advanced Theory of Statistics Vol. 2B (Edward Arnold, London, 1994).

[37] RAaij *et al.* [LHCb Collaboration], "First evidence for the decay Bs -¿ mu+ mu-," arXiv:1211.2674 [hep-ex].

[38] J. F. Gunion and H. E. Haber, "Two-body Decays Of Neutralinos And Charginos," Phys. Rev. D **37** (1988) 2515.

[39] T. Sjostrand, S. Mrenna and P. Z. Skands, JHEP **0605**, 026 (2006) [hep-ph/0603175].

[40] L. Demortier, S. Jain and H. B. Prosper, "Reference priors for high energy physics," Phys. Rev. D **82**, 034002 (2010) [arXiv:1002.1111 [stat.AP]].

[41] P. C. Bhat, H. B. Prosper and S. S. Snyder, "Bayesian analysis of multisource data," Phys. Lett. B **407**, 73 (1997).

[42] S. Chatrchyan *et al.* [CMS Collaboration], "Search for new physics in the multijet and missing transverse momentum final state in proton-proton collisions at $\sqrt{s} = 7$ TeV," arXiv:1207.1898 [hep-ex].

[43] S. Chatrchyan *et al.* [CMS Collaboration], "Search for supersymmetry in events with b-quark jets and missing transverse energy in pp collisions at 7 TeV," arXiv:1208.4859 [hep-ex].

[44] S. Chatrchyan *et al.* [CMS Collaboration], "Search for physics beyond the standard model in events with tau leptons, jets, and large transverse momentum imbalance in pp collisions at sqrt(s) = 7 TeV," arXiv:1301.3792 [hep-ex].

[45] S. Chatrchyan *et al.* [CMS Collaboration], "Search for dark matter and large extra dimensions in monojet events in pp collisions at sqrt(s)= 7 TeV," arXiv:1206.5663 [hep-ex].

[46] S. Chatrchyan *et al.* [CMS Collaboration], "Search for new physics with same-sign isolated dilepton events with jets and missing transverse energy," Phys. Rev. Lett. **109**, 071803 (2012) [arXiv:1205.6615 [hep-ex]].

[47] S. Chatrchyan *et al.* [CMS Collaboration], "Search for new physics in events with opposite-sign leptons, jets, and missing transverse energy in pp collisions at $\sqrt{s} = 7$ TeV," Phys. Lett. B **718**, 815 (2013) [arXiv:1206.3949 [hep-ex]].

[48] S. Chatrchyan *et al.* [CMS Collaboration], "Search for electroweak production of charginos and neutralinos using leptonic final states in pp collisions at sqrt(s) = 7 TeV," arXiv:1209.6620 [hep-ex].

[49] S. Chatrchyan *et al.* [CMS Collaboration], "Search for neutral Higgs bosons decaying to τ pairs in pp collisions at $\sqrt{s} = 7$ TeV," Phys. Lett. B **713**, 68 (2012) [arXiv:1202.4083 [hep-ex]].

[50] S. Chatrchyan *et al.* [CMS Collaboration], "Interpretation of Searches for Supersymmetry with Simplified Models", arXiv:1301.2175 [hep-ex].

[51] D. Alves *et al.* [LHC New Physics Working Group Collaboration], "Simplified Models for LHC New Physics Searches," J. Phys. G **39**, 105005 (2012) [arXiv:1105.2838 [hep-ph]].